

CAVITY TECHNIQUES FOR VOLUME HOLOGRAPHY

by

Bo Elliot Miller

Copyright © Bo Elliot Miller 2016

A Dissertation Submitted to the Faculty of the

COLLEGE OF OPTICAL SCIENCES

In Partial Fulfillment of the Requirements

For the Degree of

DOCTOR OF PHILOSOPHY

In the Graduate College

THE UNIVERSITY OF ARIZONA

2016

THE UNIVERSITY OF ARIZONA
GRADUATE COLLEGE

As members of the Dissertation Committee, we certify that we have read the dissertation prepared by Bo Elliot Miller, titled Cavity Techniques for Volume Holography and recommend that it be accepted as fulfilling the dissertation requirement for the Degree of Doctor of Philosophy.

_____ Date: November 15, 2016
Yuzuru Takashima

_____ Date: November 15, 2016
Thomas D. Milster

_____ Date: November 15, 2016
Milorad Cvijetic

Final approval and acceptance of this dissertation is contingent upon the candidate's submission of the final copies of the dissertation to the Graduate College.

I hereby certify that I have read this dissertation prepared under my direction and recommend that it be accepted as fulfilling the dissertation requirement.

_____ Date: November 15, 2016
Dissertation Director: Yuzuru Takashima

STATEMENT BY AUTHOR

This dissertation has been submitted in partial fulfillment of the requirements for an advanced degree at the University of Arizona and is deposited in the University Library to be made available to borrowers under rules of the Library.

Brief quotations from this dissertation are allowable without special permission, provided that an accurate acknowledgement of the source is made. Requests for permission for extended quotation from or reproduction of this manuscript in whole or in part may be granted by the head of the major department or the Dean of the Graduate College when in his or her judgment the proposed use of the material is in the interests of scholarship. In all other instances, however, permission must be obtained from the author.

SIGNED: Bo Elliot Miller

ACKNOWLEDGEMENTS

I would like to thank all those people who had a hand in training me, and supporting me throughout my PhD. studies.

Yuzuru Takashima, my advisor: though I was not always prepared do to as you asked, you still trained me to solve real problems, not just puzzles which someone else had already solved. When I first came to you, I had no experience solving real problems, or building my own experiments. I could not understand how you came up with solutions and just kept pushing forward despite not knowing everything about the task at hand. By your instruction I learned, for the first time, to apply the scientific method: hypothesizing, observing, learning and repeating. Most importantly you taught me through example how to turn on the part of my brain that learns and how to apply it a variety of situations. Thank you so much for teaching me how to learn and to teach myself.

Tom Milster, thank you for answering my random questions and providing resources with your Maskless Lithography Tool, and access to other tools. There are several sections in this dissertation that would not have been possible without your help. In particular Section 4.1.4.

To my colleagues, I offer thanks as well. Kenichi Shimada, thank you for tutoring me in the coupled wave theory of Kogelnik. Chris Summitt and Sunghin Wang, thank you for letting me bounce ideas off of me and letting me complain when things didn't go well. Jeff Brown, and Ethan Schaefer thank you for giving me Godly council in the midst of my despair.

To the instructors I TAed for and took classes with, thank you for guiding me in the periphery of my path here at Op. Sci. Masud Mansuripur, thank you for showing me how to think about mathematics. Brian Anderson, thank you for showing me the beauty of Quantum Mechanics. Scott Tyo, thank you for letting me experience the joy of classroom teaching. Matthew Kupinski, thank you for showing me that statistics and probability can be fun after all.

John Koshel, Mark Rodriguez, Amanda Ferraris, and anyone else in the academic office who had to put up with my awkward situations, thank you for supporting and encouraging me even when I was trying to quit.

I should also thank Hitachi, Ltd. for funding me, and lending me the Holoeye SLM used in my research.

Finally, I would like thank my wife encouraging me and supporting me all the way through my degree. You told me you were proud of me on many occasions, comforted me when I was angry or sad, cooked for me, worked low end jobs to supplement our income, and helped in so many small ways that I could never recall them all in life. Thank you for loving and respecting me and helping me to become a better man.

To all of you, truly, thank you for helping me to grow.

DEDICATION

As my acknowledgements attest, there are many to whom I owe thanks, and still many more that I could mention. For all the interactions and gifts given me by this great multitude there is just one person, who is yet three, to whom I dedicate this work. For it is by His divine appointment that all the smallest aspects came together in its making. Father, Son, and Holy Spirit, I dedicate this work to you, its ultimate maker, and I pray that it serve as a testament to your good work in the lives of men. Let it be known that Jesus saves all who call upon his name and follow after him, even if he must save us from the despair of graduate school.

Table of Contents

List of Figures.....	10
List of Tables	12
Abstract.....	13
1 Introduction.....	15
1.1 History of Holographic Data Storage.....	17
1.2 HDSS overview.....	17
1.3 Remaining problems in HDSS	18
1.4 Research Overview	20
2 Theoretical background	22
2.1 Volume holography and multiplexing	22
2.1.1 Mathematical formalism of holography	23
2.1.2 Angular and orthogonal phase code multiplexing	26
2.2 Optical resonator cavities	28
2.3 Summary of theoretical background	30
3 Resonant optical cavity enhanced reference beam recording	31
3.1 Theory of cavity enhanced recording.....	31
3.1.1 Theory of cavity enhanced reference beams.....	31
3.1.2 Non-cavity grating strength	33

3.1.3	Enhancement of grating strength by standing wave cavity reference beam	35
3.1.4	Enhancement of grating strength by traveling wave cavity reference beam	38
3.1.5	Cavity enhancement of write data rates in photorefractive materials	40
3.1.6	Effects of extraneous holograms on data rates and capacities.....	42
3.2	Experiments in cavity enhanced recording	45
3.2.1	Plane wave recording with a cavity enhanced reference	45
3.2.1.1	Plane wave setup and procedure	45
3.2.1.2	Plane wave results	47
3.2.2	Image recording with a cavity enhanced reference arm	49
3.2.2.1	Imaging setup and procedure	49
3.2.2.2	Imaging results	50
3.3	Discussion of cavity enhanced recording.....	53
3.3.1	Plane wave recording discussion	53
3.3.2	Elimination of extraneous holograms	57
3.4	Summary of cavity enhanced reference beam recording	58
4	Cavity enhanced orthogonal mode-angular hybrid multiplexing	60
4.1	Mode-angular hybrid multiplexing experiments	60
4.1.1	Cross-talk of single holograms read out by orthogonal cavity eigenmodes.....	60
4.1.2	Image multiplexing with Hermite-Gaussian reference beams.....	64

4.1.3	Cavity enhanced writing with Hermite-Gaussian eigenmodes.....	64
4.1.4	Combined angular and mode multiplexing with cavity enhanced writing	66
4.2	Mode-angular hybrid multiplexing discussion	67
4.3	Summary of cavity enhanced mode-angular multiplexing	71
5	Summary of contributions and suggestions on technology transfer towards commercialization.....	72
6	Conclusions and future work.....	74
	Appendix A: Publications.....	77
	Appendix B: MATLAB code for determining recording time constants	78
1	Main fitting code.....	78
1.1	MATLAB residues function	84
	Appendix C: LabVIEW code for proportional gain feedback loop.....	85
1	Main block diagram.....	85
1.1	IntToChASet.vi sub-vi	89
1.2	ReadIn0.vi sub-vi	89
1.3	MovingAverage.vi sub-vi	89
1.4	ConstrainDeltaVPZT.vi sub-vi	90
	References	91

List of Figures

Fig. 1. De-facto HDSS.....	18
Fig. 2. Wave and grating vectors for recording geometries.....	32
Fig. 3. Standing wave linear cavity used for formalization of grating strength for cavity enhanced writing.....	35
Fig. 4. Bow-tie cavity used for formalization of grating strength for cavity enhanced writing ...	39
Fig. 5. Diffraction efficiency yield plotted against splitting ratio.....	45
Fig. 6. Schematic diagram of the experimental setup of plane wave, cavity enhanced recording.	47
Fig. 7. Data and fitting curves for the best data set including a histogram of the write rate enhancements.....	49
Fig. 8. Diagram of the experimental setup for cavity image recording with an enhanced reference beam.....	50
Fig. 9. Data and fitting curves for the best imaging data set including a histogram of the enhancements.....	52
Fig. 10. Gaussian reference image reconstructions	53
Fig. 11. Fast Fourier transform of the circulating power in the cavity	56
Fig. 12. $\lambda/4$ plates are used to remove extra gratings formed in a standing wave cavity.	58
Fig. 13. Experimental setup for evaluating the cross-talk of single holograms.....	61
Fig. 14. Beam profiles for orthogonal reference beams.....	62
Fig. 15. Images for the mode multiplexing test	63
Fig. 16. Reconstructed images from HG mode multiplexing.	64
Fig. 17. Data and fitting curves for the best data set including a histogram of the write rate enhancements using a HG 1,0 reference beam.	65
Fig. 18. Pseudo-phase conjugate reconstruction of images recorded.....	67

Fig. 19. Maximum mode size (units of Gaussian beam $1/e$ field radius) as a function of the number of modes used, and storage density enhancement as a function of number of modes used.
..... 70

List of Tables

Table 1. Summary of Recording Data Rate Enhancements.....	42
Table 2. Summary of Maximum Write Data Rate Enhancements for Typical HDSS Parameters.	55

Abstract

Volume Holographic Data Storage Systems (HDSS) has been of interest for almost seven decades, and are now considered as a viable option for Write Once Read Many (WORM) cold data storage applications. Thanks to the Bragg selectivity of thick volume holograms, HDSS stores several hundreds of holograms on top of each other, called multiplexed data pages, by which data recording density can be substantially increased compared to surface recordings. On the other hand, signal intensity upon reconstruction of such multiplexed data pages inversely scales with number of multiplexing squared. Therefore, longer detection time and/or a high power laser along with a large dynamic range material is needed to make HDSS a truly viable “fast and high density” option for WORM applications. Historically, the trade-off between data density and data rate is well recognized. The challenge has been partially solved by continuous efforts such as improvement of materials, optical architectures, opto-mechanical systems and signal processing [1,2]. In this dissertation, we provide an additional pathway for HDSS to further increase both data density and transfer rates which is Cavities Enhancement Techniques for HDSS, to overcome the fundamental tradeoff.

Key ideas are: recycling light with cavity to enhance data rate, and increasing number of multiplexing by combining cavity-eigenmode multiplexing, a subset of orthogonal phasecode multiplexing, with angular multiplexing. Based on this idea, we design and demonstrate Cavity-enhanced HDSS in such a way that we increase data rate and/or data density by at least factor of 2 while taking advantage of previous improvements as they are, or only with the minimum amount of modifications.

In Section 1, we review history of HDSS and summarize the latest research results of HDSS and requirements on modern optical data storage systems as they relate to our solutions. In Section 2, theory of volume holography is reviewed by emphasizing understanding of angular and orthogonal phase code multiplexing. In Section 3 the theory of cavity enhanced reference arms is presented. We discuss how cavities provide a coherent boost to the beam power, which

can be used in recording to alleviate source power requirements and/or increase the data recording rate and demonstrate the enhancement experimentally.

Beyond basic enhancement, cavities also enable orthogonal phase code multiplexing via cavity eigenmodes. In Section 4, we experimentally demonstrate angular and orthogonal phase code hybrid multiplexing to overcome the limitation of the maximum number of multiplexing imposed by the geometrical constraints of angular multiplexing. In Section 5, novel aspects of the research are discussed in conjunction with the application of the technology for commercial use. Conclusions and future research direction are addressed in Section 6.

1 Introduction

Data storage has seen a recent market shift with the advent of cloud storage, and media streaming. Before internet speeds made remote data storage a viable option, personal and local network storage devices were tending to higher and higher capacities, but cloud storage and media streaming services have caused consumers and businesses to offload their data to remote centers. Thus, the focus in data storage development is now a challenge of designing data centers that meet the rapidly growing consumer and industrial needs remotely.

The needs of data centers are based on the “temperatures” of the data stored, and the definition of data temperature is application dependent. A familiar application would be personal computers, where the memory being actively used is read out from long term storage and kept on fast volatile memory called Random Access Memory (RAM). In personal computers, the data kept in RAM is clearly “hot”, while data remaining in long term storage is “cold”. However, data centers store much larger quantities of data with a wider range of access needs than personal computers, so it becomes meaningful to break long term storage into a continuum of hot and cold archives. In archival storage hot data must be kept in fast media to prevent speed reductions during frequent access, but cold data can be kept on slower media to reduce the total cost of ownership of data centers and reduce the possibility of data loss. Hot data’s requirement of speed has led to the use of Solid State Drives (SSD) as the fastest medium available. On the other hand, cold data is infrequently accessed or modified, but needs to be stored for long periods of time. Infrequent access coupled with the relatively high cost of SSD establishes the need to find a cheaper alternative for cold data [3].

For data temperatures between hot and cold extremes, easily rewritable and cost effective alternatives to SSD include Hard Disc Drives (HDDs) and magnetic tape drives, but the short archive life of these technologies makes them unsuitable for the coldest data. The coldest data is very stable and often immutable, so Write Once Read Many (WORM) technologies are an attractive solution. Emerging WORM technologies include the SONY/Panasonic Archival Disc (AD), Five Dimensional (5D) eternal storage, and Holographic Data Storage Systems (HDSSs).

AD is targeting a 250 GB/inch³ storage density, assuming a standard 12 disc cartridge, with a 359.65 Mbps data transfer rate and ~50 year archive life [4]. However, the scalability in data density is approaching its limit for such bit based, multi-layer optical storage. Recording densities are limited by Numerical Aperture (NA), and wavelength restrictions, as well as the problem of absorption control to maintain write and read beam transmission throughout the increasing number of recording layers [5,6]. These limitations combine to make it very difficult to reach the $1/\lambda^3$ bits/inch³ density limit of three dimensional (3D) optical data storage (on the order of 10 TB/inch³), but 5D achieves higher densities than AD simply by circumventing the 3D limit to get densities of 439 TB/inch³ and archive lives of 10²⁰ years [7]. While the 3D nature of HDSS may not be able to beat the storage density or archive life of 5D storage, HDSS can still out perform AD and 5D storage in data transfer rates due to the partially parallel access scheme of page based storage [8]. Page based HDSS also leverages multiplexing techniques by which multiple data pages are superimposed at the same location allowing for easier access to the 3D storage limit through additional Degrees of Freedom (DoF). Leveraging these techniques, current HDSS boasts 720 GB/in³ accessible at 2.4 Gpbs with a 50 year archive life, and capacities are still growing [1]. With such promising specifications HDSS considered as a viable solution for the WORM cold data storage market.

The appeal of HDSS is mainly attributed to multiplexing and parallel data transfer. AD and 5D storage both rely on multiple layers of highly localized bits, but their readout speed of the data is limited to a serial stream of bits from a given read/write head which is often limited by the maximum rotation speed of the discs. However, page based HDSS uses a single volume to store thousands of bits, thus the data transfer rate is considerably increased by the use of thousands of parallel channels. These channels come at the cost of requiring a larger recording volume in the medium, but this issue is overcome by using a multitude of reference beams to record many pages in a single volume. The reference beams can be varied in their angle and shift relative to the signal beam [9–13] and their transverse field distribution for example [14–16]. Such a diverse set of multiplexing options provides an easy means of meeting and exceeding the density of bit based optical data storage like AD.

1.1 History of Holographic Data Storage

The concept of holography began in 1948 with Gabor's work in electron microscopy [17], and was later brought to optics in 1962 by Leith and Upatnieks [18]. A year later the concept of storing data holographically was introduced until by van Heerden [7]. Following the discovery of the photo-refractive properties of LiNbO_3 and LiTaO_3 in 1966 [19], HDSS saw a boom of research based on such crystals [20–23], but such studies dwindled due to the lack of reliable tools such as lasers, Spatial Light Modulators (SLM), and digital cameras (CCD and CMOS). It wasn't until 1994 that the development of such components allowed a Stanford team to demonstrate a completely digital HDSS [24].

Following the first demonstration of digital HDSS the 1990s and 2000s saw the implementation of numerous multiplexing techniques to increase storage densities [10,12–16,25], and many new storage media were investigated including the photo-refractive crystals of the original experiments and a number of photo polymers [26,27].

During this time of active research Nintendo worked with InPhase Technologies to develop an archival HDSS [28], and in the current decade of 2010 the minds behind InPhase are continuing the development at Akonia Holographics [29]. Meanwhile, Hitachi and the Japanese Broadcasting Company (NHK) were working on their own archival HDSS [30,31]. To date the highest reported recording density of 720 GB/in^3 in a standard cartridge [1] is accomplished by using an advanced photo polymer recording medium [32], dynamic aperture angular multiplexing, quadrature homodyne detection [33], and phase quadrature multiplexing.

1.2 HDSS overview

For reference, the de-facto HDSS uses angular multiplexing as a starting point. As seen in Fig. 1, reference beams with a multitude of angles are used to record multiple holograms in a single volume. Each reference beam angle is matched with a particular signal beam. Signal beams are the Fourier Transform or near Fourier Transform of a two Dimensional array of bits called a page. The interference of each matched pair of reference and signal beams forms an irradiance

pattern inside of the recording medium. Recording mediums are photosensitive such that the exposure to light causes a change in refractive index or absorption. Refractive index modulation is preferred because it provides higher diffraction efficiencies.

With the refractive index modulation written into the recording medium, the signal beam can be recovered by illuminating with the matched reference beam angle. However, if the reference beam used to reconstruct the signal is not properly match little no diffraction efficiency will be the result. Thus, each reference beam angle can be used to store its own page.

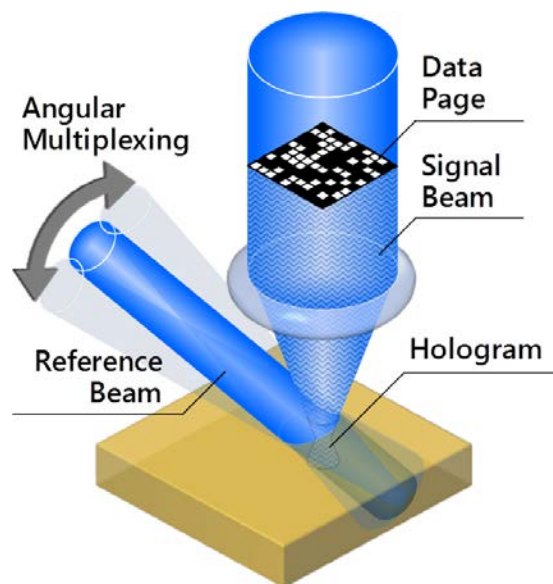


Fig. 1. De-facto HDSS. The angle of the reference beam is changed to record multiple data pages containing many bits in a single volume. The pages are Fourier Transformed, before interfering with the reference beam. The interference between the signal and reference beam is recorded as a hologram in the recording medium.

1.3 Remaining problems in HDSS

While Akonia's system specifications are competitive in the current WORM cold data storage market, further advancement in HDSS will require researchers to address three main issues. First, in order to multiplex more holograms in a given location the Bit Error Rate (BER) must be

maintained despite the trade-off in diffraction efficiencies which scale as $(M \# / N)^2$, where $M \#$ represents the material dynamic range, and N is number of multiplexed holograms [34]. Second, as the allowable number of pages increases new methods of multiplexing must be combined with those already in use to provide increasing Degrees of Freedom (DOFs) to increase the achievable number of pages toward the limits imposed by the BER. Third, recording speeds are limited by the source power and sensitivity of the recording medium.

In order to increase the data density of HDSS the maximum number of multiplexed pages must increase, but the diffraction efficiency of given page scales as the inverse square of the number of pages. Thus, increasing the number of pages decreases the BER. This issue has a number of solutions already in existence. Obvious solutions are to increase material dynamic ranges, source powers, and detector sensitivities. Less obvious solutions are advanced coding and detection schemes like quadrature homodyne detection [33], and phase shift keying [35]. Optical cavities have even been used to passively amplify the reference beam providing a quick enhancement to the source power. In readout the boosted power provides a DOF which can be used to increase storage densities, increase data transfer rates, or decrease source power requirements [36,37].

As the reduced requirement on BER by phase signal encoding allows more pages to be multiplexed, different multiplexing methods must be combined to meet the limit. Just as Akonia combined angular and phase quadrature multiplexing, angular, orthogonal phase code, shift, and wavelength multiplexing must be combined because each method has its functional limits. In particular, angular multiplexing is limited by the DOF of the maximum reference beam sweeping range of 0° to 180° , and thus is incapable of reaching the storage limit on its own. To address this limitation we propose and demonstrate a combination of orthogonal phase code multiplexing with angular multiplexing which can at least double the storage density of existing systems without imposing substantial modification.

Finally, recording speeds can only be increased by raising recording medium sensitives or increasing sources powers. As in readout, cavities provide boosted source powers with no

additional energy costs, so we propose that cavities be used on the reference beam to increase recording speeds as well.

1.4 Research Overview

As a first step, we develop a new theoretical frame work and formulas to describe the enhancement in write rate that a cavity enhanced reference beam provides, and follow the theory with an experimental demonstration. Building on this technique we use the orthogonality of cavity eigenmodes to combine angular multiplexing, orthogonal phase code multiplexing, Gaussian apodization [38], and cavity enhanced writing into a package which offers substantial increases in storage density, and data rates while requiring minimal changes in current system designs. Cavity enhanced eigenmode multiplexing was originally mentioned in Tian's work [39]. The theories of grating formation and write rate improvements are of our one of major advancements as well as demonstration of an enhanced mode multiplexing. Moreover, compatibility of cavity techniques with angular multiplexing is demonstrated for the first time.

This dissertation presents the theory necessary to apply Tian's theory to real systems, and predict actual increases in data rates and storage capacity. Following the theoretical development, this architecture is experimentally demonstrated on a simplified holographic recording setup, and its implications for the future of HDSS are discussed.

To the best of my knowledge, this is the first time cavity enhanced recording, volume holographic mode multiplexing, and cavity enhanced mode-angular hybrid multiplexing have been demonstrated experimentally. While, this research was largely inspired by Tian's work [39], we have developed the new models needed for system design as described in Sections 3.1.3 to 3.1.6. This design tool also presents a new aspect in cavity recording: the use of extra holograms created by standing wave cavities. Cao et. all performed a similar analysis and experiment using a reverse propagating reference beam to enhance recording speeds [40], but our theory and experiments are the first to demonstrate such advantages in cavity recording. Our mode multiplexing is also related to Mikami's micro-holographic mode multiplexing [41], but

this is the first demonstration of cavity enhanced mode multiplexing in volume holography. Thus, we are the first to demonstrate that cavity enhanced reference beams can increase recording speeds by 80%, and cavity enhanced mode-angular multiplexing can keep that speed while doubling the storage capacity if 5 modes are used.

2 Theoretical background

2.1 Volume holography and multiplexing

Treating light as a transverse wave in the electromagnetic spectrum we find that coherent light can be overlapped to cause interference as the field amplitudes add and subtract. When two or more coherent beams of light with the same wavelength and polarization are overlapped a static interference pattern is created. This interference pattern can be recorded in photosensitive materials as variations in the materials refractive index or absorption. The recorded pattern is a hologram which couples the two beams by the process of diffraction [42].

In order to apply holography to data storage, two beams are chosen to record the interference pattern. One is called the reference, and the other is called the signal beam which carries the information to be stored. The choice of reference allows a given signal to be matched with a given reference beam, so if the hologram is illuminated with the appropriate reference beam the diffraction of the reference beam by the hologram reconstructs the signal beam. The degree to which signals are matched to their references depends primarily on the thickness of the hologram, such that a sufficient thicknesses produce holograms in which signal and reference beams are so completely coupled that mismatched reference beams cannot read out the desired signal. This selectivity makes it possible to stack holograms with different signal and reference beam pairings in the same space in the storage material, and each signal will be retrievable provided it has been recorded with a unique reference beam. This stacking of holograms is called multiplexing, and its only requirement is a set of reference beams which are sufficiently unique for the thickness of hologram used.

There are many ways to create a unique set of reference beams, but we will focus on orthogonal phase code multiplexing [16], and the de-facto standard angular multiplexing. In angular multiplexing the thickness of the hologram gives rise to Bragg selectivity which includes a dependence of the hologram upon the angle of the reference beam. As the angle is varied from the recording beam angle the fraction of energy coupled from the reference beam to the signal

beam, diffraction efficiency, is decreased. When this diffraction efficiency is sufficiently reduced by the change in angle another hologram can be recorded at the new angle.

Moving on from angular multiplexing, in orthogonal phase code multiplexing the transverse field of the reference beams are adjusted to form a set of orthogonal beams. Because these reference beams are orthogonal, their inner products are equal to the Kronecker delta function. This results in holograms that can only be read out by the correct phase code. This chapter addresses some of the basic mathematical theory behind such multiplexed holographic recording techniques.

2.1.1 *Mathematical formalism of holography*

We begin by describing holography in terms a pair of arbitrary electromagnetic fields. Since a higher contrast interference pattern is generally desirable we also assume that the polarizations of these fields are parallel, so that they may be represented as scalar fields. The reference field, $U_R(x, y)$, and signal field, $U_S(x, y)$, inside of a thin sheet of photosensitive material are then given by

$$U_{ref}(x, y) = A_R(x, y)e^{-i\phi_R(x, y)} \quad (1)$$

$$U_{sig}(x, y) = A_S(x, y)e^{-i\phi_S(x, y)}. \quad (2)$$

Here A_S and A_R are the real valued field amplitudes of the reference and signal beam. Similarly ϕ_R and ϕ_S are the phase of the beams. The irradiance distribution, $E_e(x, y)$, in the plane of the material is then given by

$$E_e(x, y) = \frac{cn\epsilon_0}{2} |U_R + U_S|^2 = \frac{cn\epsilon_0}{2} [|A_R|^2 + |A_S|^2 + U_R^*U_S + U_R U_S^*]$$

$$= \frac{cn\epsilon_0}{2} [|A_R|^2 + |A_S|^2 + 2A_R A_S \cos(\phi_S - \phi_R)]. \quad (3)$$

Here c is the vacuum speed of light, n is the material refractive index, and ϵ_0 is the vacuum permittivity. Assuming an index changing photosensitive material, this irradiance distribution modulates the refractive index of the material. If the index change is linear with E_e we can write the transmission function of the hologram as

$$t_h(x, y) = t_{h,0} e^{-i\beta E_e(x,y)}, \quad (4)$$

where $t_{h,0}$ is the base field transmission of the material, and β is the phase response of material. If the phase modulation is small enough we can apply the weak phase object approximation to rewrite the transmission as

$$t(x, y) = t_0 [1 + i\beta \frac{cn\epsilon_0}{2} [|A_R|^2 + |A_S|^2 + U_R^* U_S + U_R U_S^*]]. \quad (5)$$

Illuminating this transmission function with the reference beam gives the field distribution at the output of the hologram:

$$U_{trans}(x, y) = U_R t_0 \left\{ 1 + i\beta \frac{cn\epsilon_0}{2} [|A_R|^2 + |A_S|^2 + U_R^* U_S + U_R U_S^*] \right\}. \quad (6)$$

Distributing the reference field over the above expression the third term in the square brackets is proportional to $A_R^2 U_S$, so that the signal recorded is now reconstructed.

In general U_R , and U_S , do not combine to create interference patterns that are easily understood or represented analytically, so it becomes meaningful to look at the holographic process for the basis functions of the Fourier Transform (FT), plane waves in \vec{r} space:

$$U_R = A_R e^{-i(\vec{\rho} \cdot \vec{r} - \omega t)} \quad (7)$$

$$U_S = A_S e^{-i(\vec{\sigma} \cdot \vec{r} - \omega t)}, \quad (8)$$

where $\vec{\rho}$ and $\vec{\sigma}$ are the reference and signal wave vectors, respectively, and wave vectors are defined as $\vec{k} = \frac{2\pi n}{\lambda_0} \hat{k}$ with λ_0 being the vacuum wavelength. Also, ω is the angular frequency of light used. Plugging these fields into the same process behind Eq. (3) we get an irradiance of

$$E_e(x, y) = \frac{cn\epsilon_0}{2} [|A_R|^2 + |A_S|^2 + 2A_R A_S \cos((\vec{\sigma} - \vec{\rho}) \cdot \vec{r})]. \quad (9)$$

From this we see that the hologram recorded by these two plane waves produces a simple cosine grating with a wave vector $\vec{K} = \vec{\sigma} - \vec{\rho}$. Assuming \vec{K} is parallel to the plane of the photosensitive material and using θ_0 as the angle between the two waves outside of material, the grating period can be written as

$$\Lambda = \frac{2\pi}{|\vec{K}|} = \frac{\lambda_0}{2n \sin(\theta_0)} \quad (10)$$

Thus arbitrary holograms can be represented as plane wave decompositions created by the amplitude of the FTs of the signal and reference fields as a function of \vec{K} and \vec{r} .

So far, we have only dealt with so called “thin” holograms, but as the thickness increase the behavior of a hologram changes considerably. Thick or thin behavior is determined by the Q-factor as it relates to hologram thickness d ,

$$Q = \frac{2\pi\lambda_0 d}{2}. \quad (11)$$

For $Q \geq 2\pi$ the hologram behaves like a thick one, and $Q < 2\pi$ is the thin regime. Equation (9) is only valid for thin holograms. For thick holograms the Bragg condition, $\vec{K} = \vec{\sigma} - \vec{\rho}$, becomes increasingly stringent in the choice of $\vec{\rho}$, such that deviations from $\vec{\rho}$ reduce the diffraction efficiency.

2.1.2 *Angular and orthogonal phase code multiplexing*

While thin plane wave holograms are appropriate for forming our understanding of hologram recording and reconstruction, they do not lend themselves easily to multiplexing; though, multiplexing has been demonstrated in micro-holograms in the non-Bragg regime [41,43]. In fact the Bragg selectivity and another property of thick volume holograms allow for easy multiplexing. The formalism generally used to study these holograms is coupled wave theory [42], which builds on the FT understanding of the previous section. In particular, constructing a diffracted field based on the work of Korzinin, followed by Bashaw's reformulation of it in a manner suitable to HDSS, produces a result where the diffraction efficiency depends on the Bragg detuning parameter $\xi(\vec{\rho}, d)$ and the cross-correlation of the recording and reconstruction reference beams in Fourier space [44–48].

Angular multiplexing takes its functionality from the Bragg detuning factor dependence. The dependence of the Bragg detuning upon the reconstruction beam angle through, $\vec{\rho}$, generally takes a functional form similar in shape to $\text{sinc}^2(\xi)$ for a wide variety of signal and reference beams. This functional dependence upon angle has local minima which are found on either side of the Bragg matched condition. Typically, angular multiplexing will choose such minima as the angular separation between reference beams. This results in increased density through

multiplexed holograms while reducing the amount that a given reference beam reconstructs holograms angularly adjacent to it, so called inter-page cross-talk.

Leaving the Bragg detuning factor, orthogonal phase code multiplexing utilizes the cross-correlation of the recording and reconstruction beams in order to build its set of reference beams. The cross-correlation of arbitrary complex functions h and g in \vec{k} space has the form of

$$(g \otimes h)(\vec{k}) = \int_{\mathbb{R}^3} g^*(\vec{k}' - \vec{k}) h(\vec{k}) d\vec{k}. \quad (12)$$

A set of orthogonal functions is defined by the scalar product integral. For a set of orthonormal functions indexed by two mode numbers we find that they satisfy the relation

$$\langle g_{n,m} | g_{p,q} \rangle(\vec{k}) = \int_{\mathbb{R}^3} g_{n,m}(\vec{k}) g_{p,q}^*(\vec{k}) d\vec{k} = \delta_{n,p} \delta_{m,q}, \quad (13)$$

where $\delta_{n,m}$ is the Kronecker delta defined as

$$\delta_{n,m} = \begin{cases} 0 & \text{if } n \neq m \\ 1 & \text{if } n = m \end{cases} \quad (14)$$

when $\vec{k}' = \vec{0}$ in the cross-correlation it is equivalent to the scalar product. Thus, for a set of orthogonal reference beams we expect that illuminating a hologram with the un-matched reference beam will produce only a very weak diffracted beam from the set of $\vec{k}' \neq \vec{0}$. In fact this cross-correlative reconstruction yields cross-talks a factor of 2 lower than that of angular multiplexing [44].

2.2 Optical resonator cavities

The same coherence properties of light which are used to record holograms can be used to increase a beam's power by overlapping it with itself in the transverse and longitudinal dimensions. To begin we start with an infinite summation of simple plane waves [49]. One can imagine an infinite plane wave captured between two infinite planar mirrors. When the mirrors are perfectly parallel to each other and the wave fronts of the plane wave, the plane wave will be sent back on itself infinitely. Relevant quantities for the summation of these oscillating plane waves include the incident field amplitude U_{in} , entrance coupler transmission coefficient t_1 , field amplitude transmission inside the cavity t_{cav} , and the round trip phase difference of the cavity δ . Thus, in the coordinate system of \vec{r} for a wave vector \vec{k} and frequency ω we can write the forward propagating field inside the cavity:

$$U_{cav}(\vec{r}, t) = U_{in} e^{i(\vec{k} \cdot \vec{r} - \omega t)} \frac{it_1}{1 - t_{cav} e^{i\delta}}. \quad (15)$$

Taking the magnitude squared of the field gives an expression proportional to the forward propagating power inside the cavity, which is also proportional to the irradiance E_e with T_1 being the entrance coupler power transmittance:

$$E_{e,cav} = E_{e,in} \left(\frac{T_1}{1 + t_{cav}^2 - 2t_{cav} \cos(\delta)} \right). \quad (16)$$

Thus, the use of a cavity in conjunction with a coherent beam can be seen to enhance the forward propagating irradiance by the quantity in the above parentheses:

$$G_F = \left(\frac{T_1}{1 + t_{cav}^2 - 2t_{cav} \cos(\delta)} \right). \quad (17)$$

Between the standing wave and traveling wave cavities the only change in G_F comes from t_{cav} . These differences will be addressed in Secs. 3.1.3 and 3.1.4.

While this analysis is completely valid for overlapping a beam with itself in the longitudinal direction, it is insufficient for transverse overlapping: the infinite plane wave is an idealized function and cannot be approximated well enough to compensate for the infinite propagation distance assumed for cavity oscillation. Thus, for the simple case of a two mirror standing wave resonator one must find a choice of mirror shapes and transvers beam field that will overcome the issues of diffraction and contain the beam completely. This is generally done by choosing spherical mirrors with different radii of curvature R_1 and R_2 and aligning them at a distance of L . The stability parameters are then given by

$$g_1 = 1 - \frac{L}{R_1} \quad (18)$$

$$g_2 = 1 - \frac{L}{R_2}. \quad (19)$$

A cavity then has stable transverse field distributions called eigenmodes if the product of the parameters obeys the relation

$$0 \leq g_1 g_2 \leq 1 \quad (20)$$

The eigenmodes thus secured take the form any number of solution family generated by solving the wave equation inside the cavity. The most well-known eigenmode families are the Hermite-Gaussians (HG) which arise from rectangularly symmetric cavities and the Laguerre-Gaussians which arise from cylindrical symmetry.

As these modes are both Gaussian in nature and derived as an orthogonal set of basis solutions to a differential equation, the FTs of such mode families are also orthogonal. As we saw in Section 2.1.2, an orthogonal set of functions can be used as reference beams to multiplex holograms with low cross-talks.

2.3 Summary of theoretical background

Beginning from a plane wave understanding of the formation of thin holograms, we see that holograms are formed by the interference two coherent beams of light inside of a photo-sensitive material. However, this plane wave thin holographic recording does not easily allow multiplexing of data pages, so we use FT and coupled wave theory to model the behavior of thick holograms. Such thick holograms display an increased degree of sensitivity to the choice of reference beam. If the reconstruction reference beam is sufficiently different from the recording reference beam reconstruction of the signal will have a low diffraction efficiency. Careful choice of these reference beams allows us to multiplex many pages in a single volume. Angular multiplexing uses the Bragg detuning factor to multiplex pages with different reference beam angles, while orthogonal phase code multiplexing uses the cross-correlation of the recording and reconstruction beams to create unique reference beams.

3 Resonant optical cavity enhanced reference beam recording

Holograms are recorded through the interference of two coherent beams, a well-known and reproducible reference beam and a data bearing signal beam. Just as the two beams interfere with each other to record a hologram, any beam can be overlapped with itself through the use of an optical cavity. If the cavity and beam are designed to perfectly overlap the beam with itself in time and space, the interference is completely constructive and the beams power is increased by the coherent addition of an infinite number of copies of itself. In this chapter such an optical cavity is applied to the reference arm of a holographic recording system to improve energy usage.

3.1 Theory of cavity enhanced recording

3.1.1 *Theory of cavity enhanced reference beams*

We can now apply the cavity enhancement described by Eq. (16) to the possible recording geometries depicted in Fig. 2. Double cavity geometries will not be considered, since a full theory of image bearing cavities has not yet been developed; however, this is good topic of future research as discussed in Section 6. We will cover the enhancement in grating strength of the single standing wave and single traveling wave geometries. To aid in visualizing the geometries considered, the beam wave-vectors and grating vectors are summarized in Fig. 2, where $\vec{\rho}$ and $\vec{\sigma}$ are the reference and signal beam wave vectors, $-\vec{\rho}$ is the reverse propagating reference beam, \vec{K}_{trans} is the desired transmission gating vector, \vec{K}_{refl} is an extraneous reflection grating, and \vec{K}_{stand} is an extraneous distributed reflection hologram.

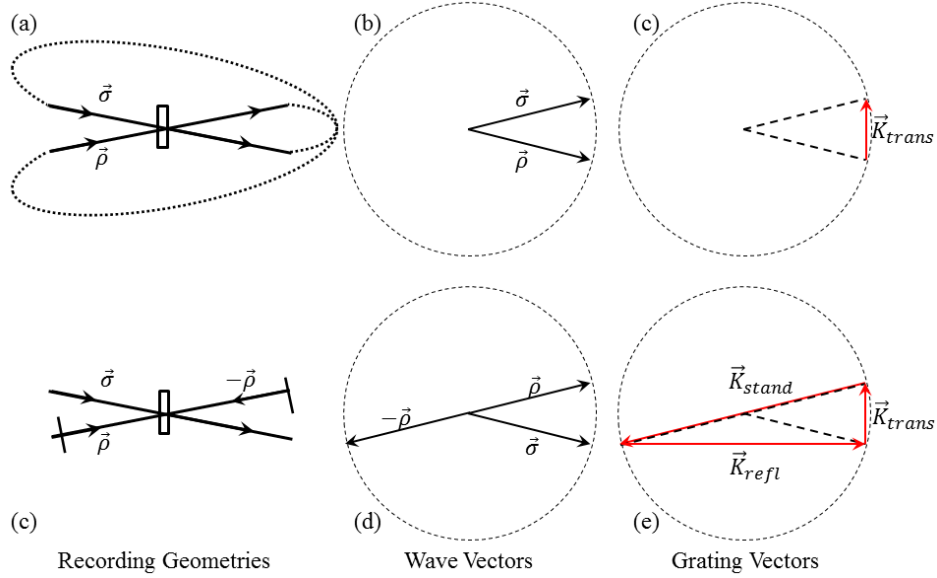


Fig. 2. Wave and grating vectors for recording geometries. (a) Recording beam geometry for normal writing as well as single and double traveling wave cavity writing. Dotted lines indicate the recirculation path of beams in traveling wave cavities. (b) Recording beam wave vectors for Fig. 2a. (c) Grating vector for Fig. 2a. (d) Recording beam geometry for single standing wave cavity writing. (e) Recording beam wave vectors for Fig. 2d. (c) Grating vectors for Fig. 2d.

Before we discuss the particular geometries, let us begin with the most general field distributions we will encounter. As seen in Fig. 2, the single and double traveling wave geometries only have two waves involved in grating formation, while the single standing wave cavity introduces a third wave to the single cavity geometry due to the collinear nature of the standing wave cavity. Thus, the most general field distribution that we will encounter is a three wave addition as follows:

$$U_{tot}(\vec{r}, t) = A_R e^{j(\vec{\rho} \cdot \vec{r} - \omega t)} + A_B e^{j(-\vec{\rho} \cdot \vec{r} - \omega t)} + A_S e^{j(\vec{\sigma} \cdot \vec{r} - \omega t)}, \quad (21)$$

where the total field in \vec{r} space for time t is U_{tot} , A_R and A_B are the forward and backward propagating reference beam amplitudes, A_S is the forward propagating signal beam amplitude, $\vec{\sigma}$ is the signal beam wave vector, and $\vec{\rho}$ is the reference beam wave vector. It should be noted

that while we have placed the cavity on the reference arm of Fig. 1, it would be equally valid to enhance the signal arm since we are working with plane wave holograms for analysis.

Taking the magnitude squared of this plane wave summation, we arrive at the general irradiance distribution of a recording geometry:

$$E_{e,tot}(\vec{r}) \propto \left[\begin{array}{c} A_R^2 + A_B^2 + A_S^2 \\ +2A_RA_B \cos(2\vec{\rho} \cdot \vec{r} - \pi) + 2A_RA_S \cos((\vec{\sigma} - \vec{\rho}) \cdot \vec{r}) \\ +2A_BA_S \cos((\vec{\sigma} + \vec{\rho}) \cdot \vec{r} - \pi) \end{array} \right]. \quad (22)$$

From Eq. (22) we can see that the three beam configuration creates three cosine terms corresponding to three gratings. The first cosine term is the grating corresponding to the standing wave of the cavity, while the second and third terms are transmission and reflection type holograms which couple the signal and reference beams. It can also be seen that there are three offset terms in the form of squared field amplitudes.

Assuming we are trying to record transmission type holograms, the only grating of Eq. (22) that we want is the second cosine term, and this grating will be our focus for simple enhanced recording. However it should be noted that, similar to the work of Liangcai Cao [40], the use of standing wave cavities is seen to consume extra dynamic range in the form of additional offset terms and unwanted gratings. The effects of these extra gratings are addressed in Section 0.

3.1.2 Non-cavity grating strength

In order to theoretically demonstrate cavity enhancement in write data transfer rate, we must first establish the base-line model for comparison. This base-line model will be simple plane wave, non-cavity recording. We begin by assuming a plain wave input of irradiance $E_{e,in}$ to be split between the two recording beams, so that we have a field amplitude of

$$A_{in} = \sqrt{\frac{2}{cn\epsilon_0} E_{e,in}}. \quad (23)$$

If we then write the irradiance splitting ratio S as

$$S = \frac{E_{e,\rho}}{E_{e,\sigma}}, \quad (24)$$

where $E_{e,\rho}$ is the irradiance of the reference arm, $E_{e,\sigma}$ is the irradiance of the signal arm, and we constrain $E_{e,\rho} + E_{e,\sigma} = E_{e,in}$, we can then write the reference and signal arm irradiances as

$$E_{e,\rho} = \frac{SE_{e,in}}{1+S} \quad (25)$$

$$E_{e,\sigma} = \frac{E_{e,in}}{1+S}. \quad (26)$$

Looking back at Eqs. (21) and (22), with $A_R = \sqrt{E_{e,\rho}}$, $A_B = 0$, and $A_S = \sqrt{E_{e,\sigma}}$ we can now write the coherent scalar field addition in the recording medium as

$$U_{tot} = \sqrt{\frac{2}{cn\epsilon_0} \frac{E_{e,in}}{1+S}} \left[\sqrt{S} e^{i(\vec{\rho}\cdot\vec{r})} + e^{i(\vec{\sigma}\cdot\vec{r})} \right], \quad (27)$$

where \vec{r} is the position vector. Taking the magnitude squared to find the irradiance distribution we get

$$E_{e,tot} = \frac{E_{e,in}}{1+S} \left[(S+1) + 2\sqrt{S} \cos((\vec{\rho} - \vec{\sigma}) \cdot \vec{r}) \right]. \quad (28)$$

To maximize the modulation depth of this irradiance distribution we set $S = 1$, equal splitting. This gives the typical form of the normal plane wave holographic recording irradiance pattern:

$$E_{e,tot} = E_{e,in} \left[1 + \cos((\vec{\rho} - \vec{\sigma}) \cdot \vec{r}) \right]. \quad (29)$$

3.1.3 *Enhancement of grating strength by standing wave cavity reference beam*

To find the grating strength enhancement of a single standing wave cavity applied to the reference arm we need to formulate the G_F of Eq. (17) and the field amplitudes of Eq. (21). Beginning with the cavity enhancement factor G_F , we find that circulating fields in a two mirror, standing wave resonator encounter losses from the mirror reflection coefficient magnitudes r_1 and r_2 , the hologram diffraction efficiency η , and the recording material absorption loss b , as shown in Fig. 2.

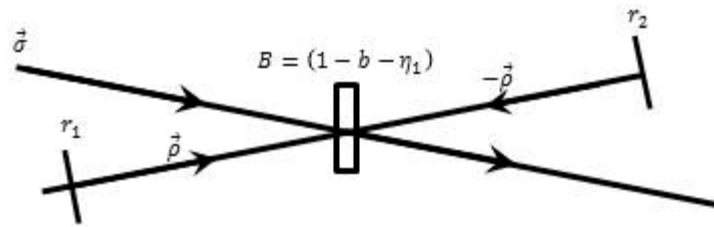


Fig. 3. Standing wave linear cavity used for formalization of grating strength for cavity enhanced writing: r_1 and r_2 are mirror reflection magnitudes, $\vec{\rho}$ is the reference wave vector, $\vec{\sigma}$ is the signal wave vector, B is the amplitude transmission for the recording material, b is the material power loss, and η_1 is the base diffraction efficiency.

Thus, we can write the cavity transmission, t_{cav} of Eq. (15), as

$$t_{cav} = r_1 r_2 (1 - b - \eta). \quad (30)$$

Here the term in parentheses is technically an irradiance transmission term, but in a standing wave resonator the round trip of the beam takes it through the recording material twice, so that taking its square root is negated. Thus, for a perfectly tuned cavity length we may write the G_F for the standing wave cavity [36]:

$$G_F = \frac{1 - r_1^2}{1 + (r_1 r_2 (1 - b - \eta))^2 - 2 r_1 r_2 (1 - b - \eta)}. \quad (31)$$

Applying Eq. (31) to the coefficients of Eq. (21) we can write the field amplitudes as

$$A_R = \sqrt{\frac{S E_{e,in} G_F}{1 + S}}, \quad A_B = \sqrt{\frac{S E_{e,in} r_2^2 (1 - b - \eta_1) G_F}{1 + S}}, \quad A_S = \sqrt{\frac{E_{e,in}}{1 + S}}. \quad (32)$$

This gives us the form of the irradiance distribution for the single standing wave cavity:

$$E_{e,tot}(\vec{r}) = \frac{E_{e,in}}{1 + S} \left[\begin{array}{c} S G_F (1 + r_2^2 (1 - b - \eta_1)) + 1 \\ + 2 S G_F \sqrt{r_2^2 (1 - b - \eta_1)} \cos(2 \vec{\rho} \cdot \vec{r} - \pi) \\ + 2 \sqrt{S G_F} \cos((\vec{\sigma} - \vec{\rho}) \cdot \vec{r}) \\ + 2 \sqrt{S G_F r_2^2 (1 - b - \eta_1)} \cos((\vec{\sigma} + \vec{\rho}) \cdot \vec{r} - \pi) \end{array} \right]. \quad (33)$$

As in Section 3.1.1, the only grating we want is the second cosine term. Comparing the grating strengths of Eqs. (33) and (29), we can see that the general enhancement in grating strength is given by

$$f(G_F) = \frac{2\sqrt{SG_F}}{1+S}. \quad (34)$$

Ideally, we would like to have unit fringe visibility where the offset terms are equal to the amplitude of this cosine term, but there is no real value of the splitting ratio that will accomplish this. Thus, it is more advantageous to maximize the grating strength of this particular term. The splitting ratio for maximum grating strength is then found by setting the derivative of the grating strength to zero and solving for the splitting ratio S:

$$\frac{\partial}{\partial S} \frac{2\sqrt{SG_F}}{1+S} = \frac{(S+1)G_F(G_FS)^{\frac{1}{2}} - 2\sqrt{G_FS}}{(S+1)^2} = 0, \quad (35)$$

which leads to,

$$S = 1. \quad (36)$$

This local extremum must be a maximum because the grating strength approaches zero as S approaches zero, as well as when S approaches infinity. Thus, we find that the grating strength of the desired hologram is maximized for a splitting ratio of unity, even splitting. This gives us an irradiance distribution of

$$E_{e,tot}(\vec{r}) = \frac{E_{e,in}}{2} \left[\begin{array}{c} G_F(1+r_2^2(1-b-\eta_1))+1 \\ +2G_F\sqrt{r_2^2(1-b-\eta_1)}\cos(2\vec{\rho}\cdot\vec{r}-\pi) \\ +2\sqrt{G_F}\cos((\vec{\sigma}-\vec{\rho})\cdot\vec{r}) \\ +2\sqrt{G_Fr_2^2(1-b-\eta_1)}\cos((\vec{\sigma}+\vec{\rho})\cdot\vec{r}-\pi) \end{array} \right]. \quad (37)$$

Comparing the grating strengths of Eq. (37) to Eq. (29) it is clear that we have a maximum enhancement of

$$f(G_F) = \sqrt{G_F}. \quad (38)$$

3.1.4 *Enhancement of grating strength by traveling wave cavity reference beam*

Starting from the definition of the cavity transmission for a traveling wave, bow-tie cavity, we can derive the form of G_F . Figure 4 shows a schematic of such a cavity where r_1 to r_4 are the magnitudes of the mirror reflection coefficients, ρ_1 to ρ_4 are the reference beam paths in the cavity, B is the roundtrip amplitude transmission for the recording material, b is the material power loss, and η is the hologram base diffraction efficiency. Here, B is the square root of the power transmission because the reference beam only passed through the material once per round trip. This gives us a round trip transmission coefficient of

$$t_{cav} = r_1 r_2 r_3 r_4 \sqrt{1 - b - \eta}. \quad (39)$$

Thus, for a perfectly tuned cavity length we may write the G_F for the traveling wave cavity:

$$G_F = \frac{1 - r_1^2}{1 + \left(r_1 r_2 r_3 r_4 \sqrt{1 - b - \eta} \right)^2 - 2 r_1 r_2 r_3 r_4 \sqrt{1 - b - \eta}}. \quad (40)$$

This gives us the form of the irradiance distribution for the single traveling wave cavity:

$$E_{e,tot}(\vec{r}) = \frac{E_{e,in}}{1+S} \left[S + G_F + 2\sqrt{SG_F} \cos((\vec{\rho} - \vec{\sigma}) \cdot \vec{r}) \right]. \quad (41)$$

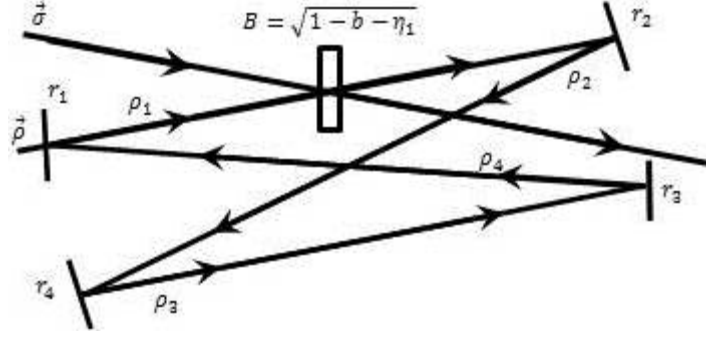


Fig. 4. Bow-tie cavity used for formalization of grating strength for cavity enhanced writing: r_1 to r_4 are mirror reflection magnitudes, ρ_1 to ρ_4 are the reference beam paths, $\vec{\rho}$ is the reference wave vector, $\vec{\sigma}$ is the signal wave vector, B is the amplitude transmission for the recording material, b is the material power loss, and η_1 is the base diffraction efficiency.

As in Section 3.1.1, we only have one cosine term which is our desired grating. Comparing the grating strengths of Eqs. (41) and (29), we can see that the general enhancement in grating strength is still given by Eq. (34). The only change is that G_F is now given by Eq. (40). Once again, we would like to have unit fringe visibility, and this time it is possible. If we set the splitting ratio to the cavity gain, $S = G_F$, we get unit fringe visibility, and we can write the grating strength enhancement as

$$f(G_F) = \frac{2G_F}{1+G_F}. \quad (42)$$

It is also important to note that since the general form of the grating strength enhancement is still given by Eq. (34), we can also choose to disregard the fringe visibility and maximize the grating strength according to Eq. (35). Maximizing grating strength at the cost of fringe visibility would be an attractive option if the constant irradiance terms of Eq. (41) do not consume

dynamic range, but losses in fringe visibility are generally considered to be undesirable if the constant terms consume dynamic range.

3.1.5 *Cavity enhancement of write data rates in photorefractive materials*

Now that we know how the grating strength is enhanced via cavities, we need to consider how these enhancements in grating strength transfer to the write rate. We analyze write rate enhancement with photorefractive materials such as Fe:LiNbO₃. We begin by defining a functional form for the time evolution of a hologram based on the band transport equations in photorefractive materials, and the coupled wave equations [50,51]. Under the band transport model the refractive index modulation depth, n_1 , evolves in time according to a simple differential equation:

$$\frac{dn_1}{dt} = -\frac{n_1}{\tau} + \frac{n_{ss}}{\tau}, \quad (43)$$

where τ is the photorefractive time constant, n_{ss} is the steady-state or saturation index modulation, and t is the exposure time. Adding the coupled wave equations to this analysis alters the functional form of n_{ss} so that it is no longer constant, but varies with time [50]. However, this time variation is due to transient energy transfer between the recording beams, thus n_{ss} remains constant when the signal and reference beams have the same irradiance. This is the case for our non-cavity writing experiments, but recording beam irradiances are not equal during our single cavity recording trials.

During our single cavity recording experiments, the available power is split equally between the cavity and non-cavity beam, and the cavity beam is enhanced by a factor of 2. This will result in a time dependent n_{ss} which depends on the energy exchange of the unbalanced beams. Heaton et. all analyzed this transient behavior by solving the coupled equations. An iterative, numerical method was used, where each time step used a version Eq. (43) to solve for the instantaneous

refractive index modulation. The intermediate solution was used to solve for the new beam irradiances [51]. This indicates that for exposure times $t \ll \tau$ the time dependence of n_{ss} may be ignored. Thus, for $t \ll \tau$ we may write the time dependence of the refractive index modulation depth as

$$n_1(t) = n_{ss} (1 - e^{-t/\tau}). \quad (44)$$

The assumption of $t \ll \tau$ is justified in Section 3.2.1.1, so that we now have a functional form for the time dependence of the refractive index modulation depth. We can apply this form to Kogelnik's Eq. 45 to arrive at an equation for the time evolution of diffraction efficiency [42]:

$$\eta(t) = \sin^2 \left(A (1 - e^{-t/\tau}) \right), \quad (45)$$

where A is a constant dependent upon n_{ss} , the grating thickness, recording wavelength, and Bragg angle. A is independent of recording irradiance for continuous wave recording [52] and τ is linearly dependent on irradiance [50,52], so the enhancement in write rate is applied to τ . Thus, the enhancement of write-rate can be computed by taking the ratio of the non-cavity recording time constant to the cavity recording time constant. These ratios will theoretically follow the grating enhancements derived in Section 3.1.3 and 3.1.4, and are summarized in Table 1.

Table 1. Summary of Recording Data Rate Enhancements.

Recording Geometry	Write Data Rate Enhancement: $f(G_F)$
Normal	1
Single Standing Wave Cavity	$\sqrt{G_F}$
Single Traveling Wave Cavity	$\frac{2G_F}{1+G_F} \cdot \sqrt{G_F}$

3.1.6 *Effects of extraneous holograms on data rates and capacities*

According to Section 3.1.1, using a standing wave cavity to enhance the reference beam adds two additional gratings to the plane wave recording geometry by adding a counter propagating reference beam. An extra plane wave grating corresponds to an extra hologram in image recording scenarios. According to Fig. 2 the two gratings are a signal bearing reflection type hologram \vec{K}_{refl} and a distributed Bragg grating, \vec{K}_{stand} , containing only information about the reference beam. One could get rid of the standing wave by using a traveling wave resonator or quarter wave plates as in Section 3.3.2, but this would also get rid of the signal bearing reflection type hologram.

Since the standing wave cavity creates two signal bearing holograms instead of one, we can expect an additional increase in the recording speed at the cost of dynamic range consumed by the standing wave hologram. This loss of dynamic range may not be desirable, but the further increase in write rate may make it worth the loss.

It should be noted that the effect these additional gratings was not observed in our experiments due to the nature of the Fe:LiNbO₃ crystal and the orientation of the c-axis relative to the grating vectors. Since the c-axis was aligned perpendicular to the reference beam, the extra gratings were oriented near perpendicular to the c-axis. While this arrangement would still allow the gratings to consume the dynamic range of the crystal, the electro-optic effect of the crystal did not cause refractive index changes to couple the recording waves [53].

However, when the recording medium can support the extra gratings, such as a photo polymer, we produce gratings according to the irradiance pattern of Eq. (33). Similarly Eq. (28) defines the grating strengths of holograms recorded in the normal way. Since the time evolution of a hologram is directly related to the irradiance of its interference pattern we can compute the ratio of the dynamic range consumed in signal recording to the dynamic range consumed by the unwanted terms like the constant offset and standing wave hologram. We will call this figure of merit the diffraction efficiency yield. For non-cavity writing the yield looks like

$$Y_{non} = \frac{2\sqrt{S}}{1+S+2\sqrt{S}}. \quad (46)$$

Similarly, if we let $B_r = R_2(1 - b - \eta_1)$, the yield of single standing wave recording is

$$Y_{cav} = \frac{(1 + \sqrt{B_r})}{1 + \sqrt{B_r} + \frac{1}{2}\sqrt{G_F S} + \sqrt{B_r G_F S} + \frac{1}{2}B_r \sqrt{G_F S} + \frac{1}{2\sqrt{G_F S}}}. \quad (47)$$

Both yields max out at 0.5, which corresponds to unit fringe visibility in non-cavity recording, but cavity writing has its maximum at smaller values of S due to the cavity enhancement. The analytic form of the optimum splitting ratio for cavity yield is

$$S_{max,cav} = \frac{1}{G_F(1 + 2\sqrt{B_r} + B_r)}. \quad (48)$$

Using that optimum splitting ratio we arrive at Write Rate Enhancement (WRE) of

$$WRE_{opt,local} = \sqrt{G_F}(1 + \sqrt{B_r}) \quad (49)$$

when comparing cavity and non-cavity writing at the same splitting ratio. However, if we compare write rates at the respective maximum yield splitting ratios, $S_{max,cav}$ for the cavity and $S = 1$ for non-cavity, we see an optimal WRE of

$$WRE_{opt,global} = \frac{(2G_F(\sqrt{B_r} + 1)^2)}{G_F + 2\sqrt{B_r}G_F + B_rG_F + 1} \quad (50)$$

As a point of reference we look at the optimal splitting ratio and WRE for our experimental setup in Section 3.2.2.2: $G_F \cong 1.48$, $R_2 = 0.99$, $b = 0.139$, and η_1 is assumed small enough to ignore compared to b . In this case $S_{max,cav} = 0.183$ gives us $WRE_{opt,local} = 2.34$ and $WRE_{opt,global} = 1.69$. Both of these WREs are improvements over conventional writing as well as the cavity enhancement described in Section 3.1.3 and 3.1.4. This increase in diffraction efficiency yield is shown graphically in Fig. 5. Also, applying the system losses describe in Section 3.3.1, we see that WRE increases from 1.6 to 1.81 by leveraging the additional grating.

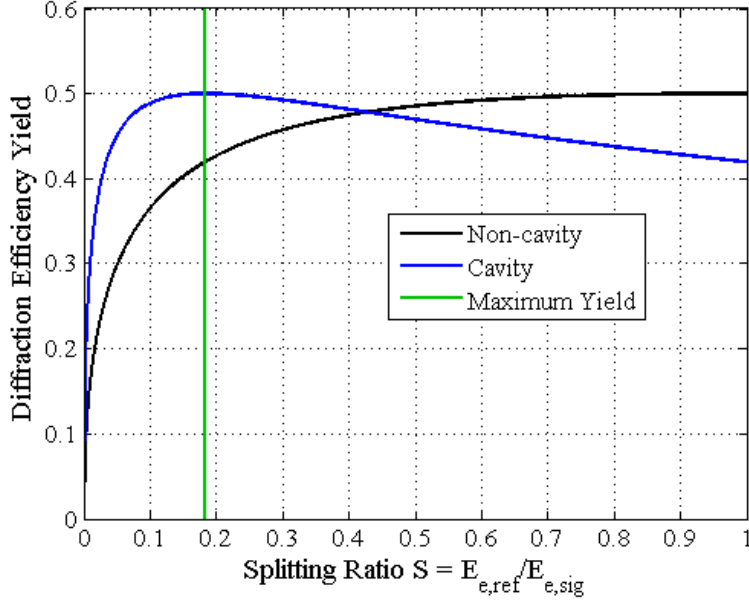


Fig. 5. Diffraction efficiency yield plotted against splitting ratio for $G_F \cong 1.48$, $R_2 = 0.99$, $b = 0.139$, and $\eta_1 \cong 0$. This gives $S_{max,cav} = 0.183$, $WRE_{opt,local} = 2.34$, and $WRE_{opt,global} = 1.69$.

3.2 Experiments in cavity enhanced recording

3.2.1 Plane wave recording with a cavity enhanced reference

3.2.1.1 Plane wave setup and procedure

As mentioned in Section 3.1.5, we work on times scales such that $t \ll \tau$. To prove this we compare our experimental setup to that of Maxein et. all [52]. For our experiments we used a combined recording irradiance of approximately 2 kW/m^2 and an Fe doping concentration in LiNbO_3 of 0.015 mole%. For a recording irradiance of 2 kW/m^2 and a doping concentration on the order of 0.1 mole%, Maxein et. all demonstrated a time constant of ~ 300 sec. Since our doping concentration is an order of magnitude lower we would expect our time constant to similarly increase to the order of at least 1×10^3 sec. Thus, Eq. (44) is applicable to our experimental results for exposure times on the order of 10 sec.

Next, to prove that single cavity enhancement of write-rates is possible we compared the photo-refractive time constants of normal and single cavity recording. To do this we wrote single holograms in an anti-reflection coated, 0.015 mole % Fe:LiNbO₃ crystal from Deltronic Crystal Industries using a diode pumped Nd:YAG laser operating with a single longitudinal mode at a 532 nm wavelength (Compass 315M, Coherent, Germany). The time evolution of the diffraction efficiency was monitored by a 633 nm wavelength He-Ne laser which was optically chopped at 80 Hz to allow for lock-in amplification of the diffracted beam using a lock-in amplifier (Model 5210, Princeton Applied Research). A single trial is composed of two holograms recorded at adjacent locations laterally separated by 1.5 mm in the crystal, so that the A term of Eq. (45) is not changed by writing successive holograms at the same location. One hologram in the set is recorded using normal methods, while the other is recorded with the reference beam which is irradiance enhanced by a 100 mm long standing wave cavity with a planar entrance coupler and a 100 mm radius of curvature, concave, mirror. Switching from cavity recording to normal recording is accomplished by flipping the entrance coupler out of the beam path and blocking the spherical mirror. Each hologram was started with a 30 sec pre-exposure to allow for alignment of the read beam to the hologram. No time evolution data was collected during this exposure, so data collection starts from 30 sec. in the data displayed in Fig. 6 in Section 3.2.1.2. To compensate for fluctuations in readout power and errors in Bragg tuning of the read beam, each data set is normalized by the read beam power and scaled by the diffracted power measured after recording the hologram and retuning the read beam. Writing beams of 532 nm wavelength and $\sim 36.5 \mu\text{W}$ power record a hologram inside an AR coated, 5x10x20 mm, 0.015 mole % Fe:LiNbO₃ crystal. The writing beams have an estimated diameter of $\sim 206 \mu\text{m}$ inside the crystal, and are separated by a 28.1° angle outside of the crystal. The 633 nm read beam has a power of $\sim 2.3 \mu\text{W}$, is chopped at 80 Hz, and has an estimated beam diameter of $\sim 291 \mu\text{m}$ inside the crystal. The standing wave cavity is formed by a 1 inch diameter, 41.8 % transmission, planar, entrance coupler, and a 1 inch diameter, 100 mm radius of curvature, 99% reflectance, dielectric mirror. The circulating power of the cavity is monitored via a 1 inch diameter beam sampler with 94% transmission. The light reflected off of that beam splitter is monitored via a photodiode

(DET110, Thorlabs) connected to a Tektronix TDS220 oscilloscope. By monitoring the oscilloscope signal, while scanning the cavity length with the Piezo-Electric Transducer (PZT) mirror mount, alignment of the cavity mirrors was tuned to maximize the cavity finesse. Prior to writing a cavity enhanced hologram, the cavity length is tuned via a constant voltage applied to the PZT. To aid in Bragg matching the readout beam, before each data set is recorded, a weak hologram is written with a 30 second exposure, and the diffraction efficiency of the read beam is maximized by adjusting its angle. Diffracted readout power is monitored via a lock-in amplified photo diode. For non-cavity recording trials the entrance coupler is flipped out of the beam path and the spherical mirror is blocked. This procedure's apparatus is shown in Fig. 6.

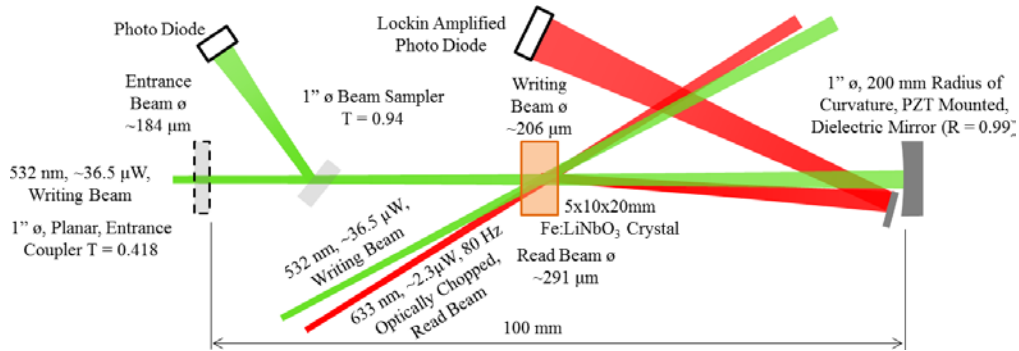


Fig. 6. Schematic diagram of the experimental setup of plane wave, cavity enhanced recording.

3.2.1.2 Plane wave results

Taking the scaled data from Section 3.2.1.1, a conversion factor is applied to convert it from a 633 nm wavelength diffraction efficiency to a 532 nm wavelength diffraction efficiency. This conversion factor was derived from averaging the ratio of the two wavelength diffraction efficiencies for twelve holograms recorded after the original data set. With the data now in units of 532 nm diffraction efficiency, we then fit the data to Eq. (45) with a least squares non-linear regression with the MATLAB coed found in Appendix B to find an average value for A of ~ 7 . Using this fixed value of A we then fit the data again while only varying τ . The write-rate enhancement of each trial pair was then computed by taking the ratio of the time constants.

Taking all eleven pairs resulted in an average enhancement of 1.07 with a standard deviation of 0.1, a maximum of 1.2, and a minimum of 0.9. However, this mean is brought down by trials which showed no enhancement or a loss in write-rate, so it becomes meaningful to look at the average of those pairs which display an enhancement greater than 1.1. There are five such trials, which give us an average of 1.16 with a standard deviation of 0.05. Fig. 7 shows the diffraction efficiency data and fitting curves for the best trial with a 1.22 enhancement in write rate, and includes a histogram of the write rate enhancements for the 11 trials. The histogram shows that recording speeds were generally enhanced, but some trials with de-enhancement were present.

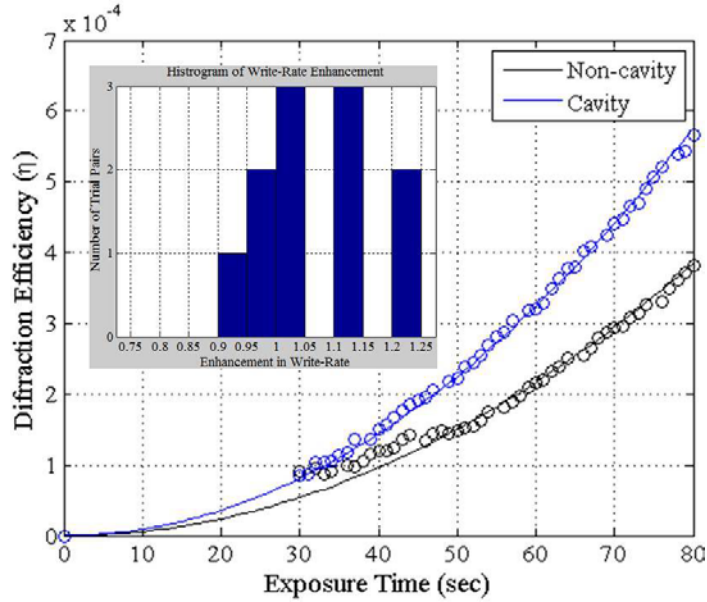


Fig. 7. Data and fitting curves for the best data set including a histogram of the write rate enhancements. The non-cavity and cavity diffraction efficiency data have time constants of 2.86×10^4 sec., and 2.34×10^4 sec., which yield a 1.22 enhancement in write data rate. The inset shows a histogram of write rate enhancements for the eleven trial pairs.

3.2.2 *Image recording with a cavity enhanced reference arm*

3.2.2.1 Imaging setup and procedure

Since an image bearing hologram cannot be fully Bragg matched with a reconstruction wavelength that differs from the recording, we changed to recording with a cavity in the reference arm and readout by a pseudo phase conjugate method similar to Cao et. all [40]. The reverse propagating beam in the standing wave cavity is used to read out the hologram while recording it.

Fig. 8 shows the experimental setup. In lieu of a data encoded bitmap pattern, we used a USAF-1951 resolution test target (Model RES-1, Newport) as the object. The object was placed at the front focal plane of a microscope objective lens (80.3020, Rolyn Optics) with $f=53$ mm, and the rear focus of the lens overlapped with the reference beam inside of the crystal. The object was illuminated by a ~ 5 mm diameter Gaussian beam. Diffraction efficiency was monitored via

the phase conjugate diffraction from the hologram being recorded which was sampled with a bare microscope cover glass inserted between the object and Fourier Transform (FT) lens. The sampled diffraction was then optically chopped and lock-in amplified by a photodiode. At the end of each recording the normal diffraction efficiency was measured without the cavity, and these measurements were used to convert the data from voltages to actual diffraction efficiencies. The reconstructed image was obtained by placing a CMOS camera (DCC1445M, Thorlabs) at the focal plane of the FT lens during reconstruction, and the object was recorded by taking a picture of the signal beam at a large distance from the focal plane of the FT lens. The reference cavity was also stabilized by a proportional gain feedback loop tied to the PZT mirror and intra-cavity power. See Appendix C for the LabVIEW code used to drive the feedback loop.

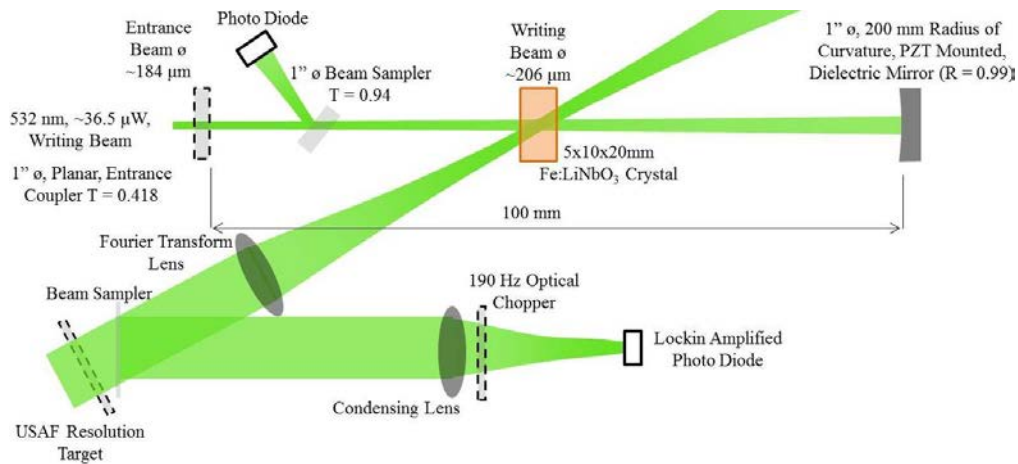


Fig. 8. Diagram of the experimental setup for cavity image recording with an enhanced reference beam.

3.2.2.2 Imaging results

To convert the voltage data from the lock-in amplifier to actual diffraction efficiencies it is scaled according to Eq. (51):

$$\eta_1(t) = \frac{1-b}{2} \left(1 - \sqrt{1 - \frac{4V(t)}{P_{ref}R_2(1-b)^2\alpha}} \right). \quad (51)$$

Here, $\eta_1(t)$ is the diffraction efficiency, b is the absorption of the crystal, $V(t)$ is the voltage data, P_{ref} is the input reference beam power, R_2 is the power reflectance of the spherical mirror, and α is a scaling factor determined for each data set according to Eq. (52):

$$\alpha = \frac{V_{max}}{P_{ref}R_2\eta_{max}(1-b-\eta_{max})}. \quad (52)$$

Here V_{max} is the maximum voltage recorded from the lock-in amplifier for the trial, and η_{max} is the diffraction efficiency recorded at the end of each trial. This data is fit with Eq. (45) to find the time constant τ with which the diffraction efficiency grows. Three trial pairs were carried out as described in Section 3.2.2.1 with the reference arm irradiance enhanced by a factor ~ 1.48 . The mean write rate enhancement of the three trials is 1.19 with a standard deviation of 0.1, which is $\sim 98\%$ of the expected 1.22. Fig. 9 displays the diffraction efficiency data for the best trial pair and a histogram showing the distribution of write rate enhancements.

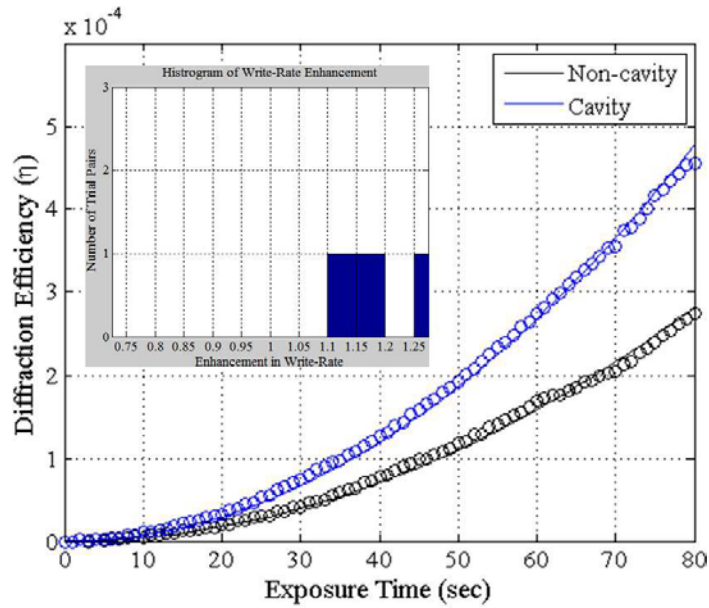


Fig. 9. Data and fitting curves for the best imaging data set including a histogram of the enhancements. The non-cavity and cavity diffraction efficiency data have a time constants of 3.34×10^4 sec., and 2.57×10^4 sec, which yield a 1.30 enhancement in write data rate. The inset shows a histogram of write rate enhancements for the three trial pairs.

A representative pair of object and reconstruction images is shown in Fig. 10. The object is seen to be clearly reconstructed from the recording created with a 1.54 irradiance enhanced reference beam. We would expect a write rate enhancement of 1.24.

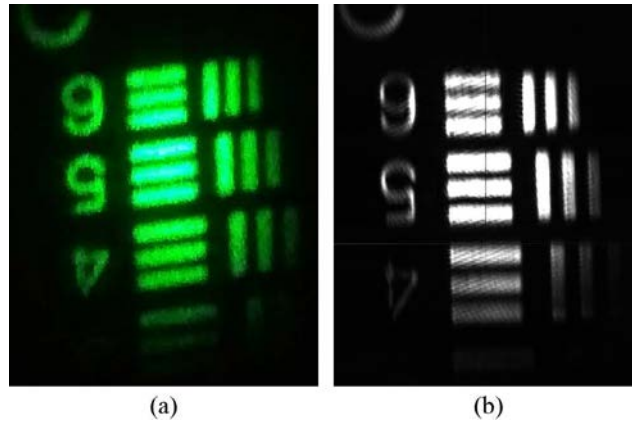


Fig. 10. Gaussian reference image reconstructions: (a) Object recorded: Newport USAF-1951 RES-1 group 1 elements 4 through 6. Maximum spatial frequency shown is 3.56 lp/mm. (b) Reconstruction recorded with a 1.54 enhanced reference arm, anticipated write rate enhancement is 1.24.

3.3 Discussion of cavity enhanced recording

3.3.1 *Plane wave recording discussion*

Returning to the theoretical discussion of Section 3.1.1, it is clear from Eqs. (31) and (40) that the cavity enhancement of irradiance is limited by the losses of the cavity. In particular G_F is inversely related to the hologram diffraction efficiency. This relationship is advantageous for HDSS where several hundred holograms are typically multiplexed to constrain individual hologram diffraction efficiencies to less than 0.3% [2,54]. Comparing the diffraction efficiency loss to the recording medium absorption (typically on the order of tens of percent), the diffraction efficiency makes a negligible change to the enhancement in write data rate. This makes cavity enhancement of holographic processes particularly well suited to HDSS, but recording medium absorption must be balanced against the cavity enhancement for maximum performance.

A natural limitation of cavities is their need for extreme stability. Generally, high values of G_F require that the cavity length be controlled with a sub 100th wave tolerance over the duration of a single hologram exposure. This requires the use of an environmental enclosure, vibration isolation table, and high-speed automated control of the cavity length for long exposure times.

Fortunately, exposure times for HDSS are on the order of 3 ms and decreasing [2], so the cavity only needs to be stabilized over a millisecond time scale allowing the system to be un-stabilized during down time and reducing the overall stabilization need.

Stability aside, let us consider the theoretical limits on cavity enhancement for typical HDSS parameters. If we design our cavity to be critically coupled [36] the entrance coupler has a power reflectance equal to the product of the remaining loss terms in the cavity, so for a standing wave cavity the maximum irradiance enhancement of Eq. (31) becomes

$$G_F = \frac{1 - (r_2(1-b-\eta))^2}{1 + (r_2(1-b-\eta))^4 - 2(r_2(1-b-\eta))^2}, \quad (53)$$

and for a traveling wave cavity the enhancement of Eq. (40) becomes

$$G_F = \frac{1 - (r_2 r_3 r_4 \sqrt{1-b-\eta})^2}{1 + (r_2 r_3 r_4 \sqrt{1-b-\eta})^4 - 2(r_2 r_3 r_4 \sqrt{1-b-\eta})^2}. \quad (54)$$

Assuming a power reflectance for the remaining mirrors of $r^2 = R = 0.99$; applying medium losses of $b = 0.2, 0.1, \text{ and } 0.05$; and a diffraction efficiency of $\eta = 0.003$; we find that the maximum irradiance enhancement for the standing and traveling wave cavities is 2.7 and 4.4 for $b = 0.2$; 4.9 and 7.7 for $b = 0.1$; and 8.9 and 12.3 for $b = 0.05$. We can now tabulate the maximum write-rate enhancements for a typical HDSS in Table 2.

Table 2. Summary of Maximum Write Data Rate Enhancements for Typical HDSS Parameters.

Recording Geometry	Write Data Rate Enhancement: $f(G_F)$		
	$b = 0.2$ (20% loss)	$b = 0.1$ (10% loss)	$b = 0.05$ (5% loss)
Normal	1	1	1
Single Standing Wave Cavity	$\sqrt{G_F} \approx 1.6$	$\sqrt{G_F} \approx 2.2$	$\sqrt{G_F} \approx 3$
Single Traveling Wave Cavity	$\frac{2G_F}{1+G_F} \approx 1.6, \sqrt{G_F} \approx 2.1$	$\frac{2G_F}{1+G_F} \approx 1.8, \sqrt{G_F} \approx 2.8$	$\frac{2G_F}{1+G_F} \approx 1.8, \sqrt{G_F} \approx 3.5$

From Table 2 we can see that cavity enhancements are very sensitive to the losses introduced by the recording medium. According to Gleeson et. al, the primary means of adjusting the absorption of photopolymers is to vary its thickness and doping concentration [55]; however, adjusting the thickness will change Bragg selectivities while changing the absorption will directly affect the sensitivity. Thus, cavity enhancement is subject to some trade-offs while providing additional degrees of freedom for system design.

Experimentally, our cavity was under coupled, $r_1 < r_2(1-b-\eta)$, and we had a system with $r_2^2 = R_2 = 0.99$, $b = 0.16$, $\eta \cong 4 \times 10^{-4}$, and $r_1^2 = R_1 = 0.572$. We also had an additional transmission loss, $t_{smp}^2 = T_{smp} = 0.94$, due to the beam sampler in the cavity so that we would expect a maximum G_F of

$$G_F = \frac{1-r_1^2}{1+(r_1 r_2 T_{smp} (1-b-\eta))^2 - 2r_1 r_2 T_{smp} (1-b-\eta)} \cong 2.8. \quad (55)$$

We managed to tune the system to $G_F \cong 2$, which is 71% of the prediction. This discrepancy is likely due to the presence of other losses in the cavity such as poor coupling or surface imperfections in the optical elements. We would expect similar reductions in G_F for implementation in photopolymer based HDSS systems where non-idealities such as scattering, shrinkage, and media vibrations [56,57] will introduce their own losses in the cavity. However

our crystal recording medium is much thicker than the interaction length of the holograms recorded, so losses could be further reduced by using a thinner crystal.

Further deviations from theory were observed: with $G_F \cong 2$ we expected a write data rate enhancement of 1.41, but saw a maximum of 1.2 with multiple trials showing no enhancement or a decrease in data rate. This performance degradation over long exposures (tens of seconds) can be attributed to the instability of the cavity: these trials were done on a vibration isolation table with no enclosure around the cavity and no cavity length stabilization. To characterize the degree of instability, the sampled and fast Fourier transformed photo diode voltage, which monitors the circulating power inside the cavity, is plotted in Fig. 11.

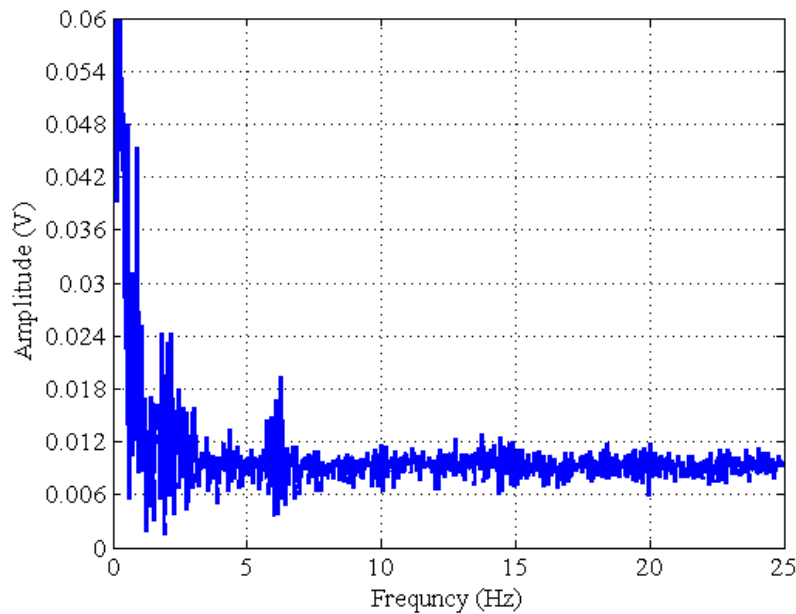


Fig. 11. Fast Fourier transform of the circulating power in the cavity as monitored by the beam sampler photo diode. This shows cavity length oscillations with frequencies around 2 Hz and 6.4 Hz.

Figure 11 clearly shows cavity length oscillations around 2 Hz and 6.4 Hz indicating the presence of slow cavity instabilities during recording. It should also be noted that the sampling interval for Fig. 11 was 20 ms, so we have no information about higher frequency instabilities;

however, both high and low frequency instabilities may be eliminated by actively tuning the cavity length. If the instabilities are only at such low frequencies the sub 3 ms exposures of current generation HDSS [2] may not require stabilization. That being said, a proportional gain feedback loop to stabilize the cavity and an enclosure to isolate system from environmental disturbances were used in the image recording of Section 3.2.2, and system performance was greatly improved.

Challenges aside, cavity enhanced reference beams can be integrated into the current monocular optical system design [58] by building the entrance coupler in to the optical system and building the rest of the cavity around the optical disc. The standing wave cavity is also compatible with pseudo-phase conjugate readout [8], and the presence of the extraneous holograms as mentioned in Section 0, with the tuning of Fig. 5 will provide an additional increase in write rate.

3.3.2 *Elimination of extraneous holograms*

The extraneous holograms created by using a standing wave cavity enhanced reference beam can be removed by switching to a traveling wave cavity, but one could also place the recording medium between two $\lambda/4$ plates to prevent the reverse propagating reference beam from interacting with the original signal and reference beams [59]. This would take the form of Fig. 6 where the reference beam entering the cavity is circularly polarized. Before entering the recording medium the light is converted to a linear polarization by a $\lambda/4$ plate. This forward propagating light in the medium has a polarization parallel to that of the signal beam. After the medium, the beam passes through a second $\lambda/4$ plate with its fast axis rotated 45° relative the direction of the linear polarization, and is converted into circular polarization. Upon reflection the beam changes handedness so that it passes back through the $\lambda/4$ plates and medium in a polarization state orthogonal to that of the forward propagating beam. Since orthogonally polarized light cannot interfere there are no additional gratings formed by the revers propagating beam. It should be noted that this technique will only work for isotropic media because any

birefringence will cause the orthogonal polarizations to deviate from each other on successive paths in the cavity which would destroy resonance.

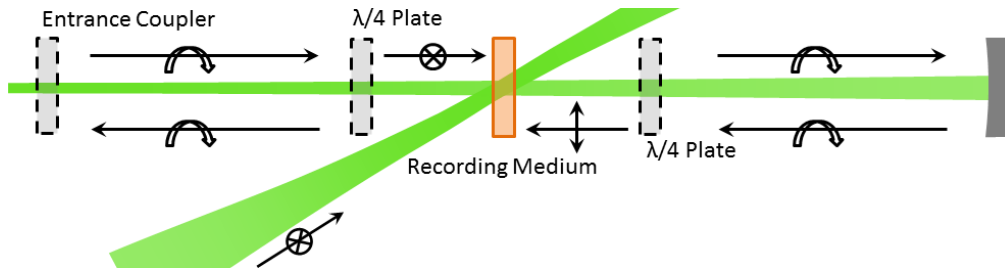


Fig. 12. $\lambda/4$ plates are used to remove extra gratings formed in a standing wave cavity. Orthogonal polarization of the forward and reverse propagating beams prevents the formation of additional holograms due to the reverse propagating reference beam.

3.4 Summary of cavity enhanced reference beam recording

We define a theoretical model for the enhancement of hologram irradiance patterns when standing and traveling wave cavities are applied to the reference arm of HDSS. Assuming that only one of the three holograms of a standing wave cavity system is recorded, write data rates can be enhanced by a factor of the square root of the cavities irradiance enhancement. Including all three holograms, and accounting for the dynamic range consumption of all of them we find that the appropriate choice of power splitting between reference and signal beam can further increase recording speeds by using an additional data bearing reflection type hologram. To test the theory, the cavity enhanced recording of a single image bearing hologram with a standing wave cavity enhanced reference arm is experimentally demonstrate with $\sim 98\%$ of the expected 1.22 factor of improvement in write rate.

Using reasonable system parameters write-rates can be enhanced by as much as a factor of 1.6 if only one of the expected gratings of standing wave cavity recording is present, but further increases are possible if the extra reflection type hologram is utilized.

While, the standing wave cavity provides considerable gains in write-rate, we must also consider the stability requirements of the cavity. The results from Section 3.2.2 were obtained

with a proportional gain feedback loop to stabilize the cavity length and an environmental enclosure to remove environmental effects. Shorter exposure times may reduce the requirement on this stability, but active and passive stabilization will be needed to maintain cavity enhancement.

4 Cavity enhanced orthogonal mode-angular hybrid multiplexing

The idea of using orthogonal phase codes to multiplex image bearing holograms has been studied well [16,41], but using cavity enhanced eigenmodes as reference beams is a novel experiment. As will be discussed in Section 4.2, the utility of eigenmode multiplexing is limited by the transvers mode shape and dimensions, so it is combined here with angular multiplexing to provide an additional DOF in increasing the storage density of HDSS. An alternative way of looking the hybrid mode-angular multiplexing, as in Section 0, is that an additional DOF is needed in angular multiplexing because the current DOFs of angular multiplexing are limited by the maximum reference beam scanning range of 0° to 180° . Angular multiplexing cannot reach the 3D storage limit on its own and neither can mode multiplexing. Thus both multiplexing schemes are incapable of reaching the storage limit on their own. To address this limitation we propose and demonstrate a combination of orthogonal phase code multiplexing with angular multiplexing which can at least double the storage density of existing systems while imposing minimum system modification.

4.1 Mode-angular hybrid multiplexing experiments

4.1.1 *Cross-talk of single holograms read out by orthogonal cavity eigenmodes*

The orthogonality of image bearing holograms is tested by using Hermite Gaussian (HG), optical cavity, eigenmodes as write reference beams [60]. We record a single image bearing hologram at its own location in the crystal by either an HG 0,0 or an HG 1,0 reference beam. The image is reconstructed with one of the two orthogonal beams and the diffraction efficiencies are compared when the hologram is read out with each beam. Cross-talk is evaluated by taking the ratio of the diffraction efficiency of the matched reference beam to that of the orthogonal reconstruction beam.

As seen in Fig. 13 an SLM (Model LC 2012, Holoeye, Germany) is setup in the reference arm of a holographic recording geometry and illuminated with a 532 nm wavelength beam from

a frequency doubled Nd:YAG laser (Compass 315M, Coherent). The recording setup is downstream of a 340 mm focal length lens. This lens Fourier Transforms (FT) the reference beam from the SLM with an additional phase and scaling factor [61]. The linear polarizers and $\lambda/2$ plates around the SLM are set to operate the SLM in the “mostly phase” modulation mode [62]. The reference beam then passes through the beam sampler, which is used in the trials of Section 3.2.2 and 4.1.3 for enhancement monitoring. The signal arm expands a Gaussian beam to a collimated beam with an approximate diameter of 5 mm. This collimated signal beam passes through the transmissive object to be recorded. The transmissive object is then Fourier Transformed by a microscope objective lens with $f = 53\text{mm}$ (Model 80.3020, Rolyn Optics). The two beams intersect inside of a 0.015 mole % Fe:LiNbO₃ crystal (Deltronic Crystal Industries, Inc.) with its c-axis perpendicular to the reference beam and parallel to the plane of the recording beams. Upon readout of the hologram a CMOS camera (DCC1445M, Thorlabs) is placed in the readout beam to record the reconstructed image. Diffraction efficiency is also measured at this point with a power meter (Newport 1918-R unit with a 918D-SL-OD3 detector).

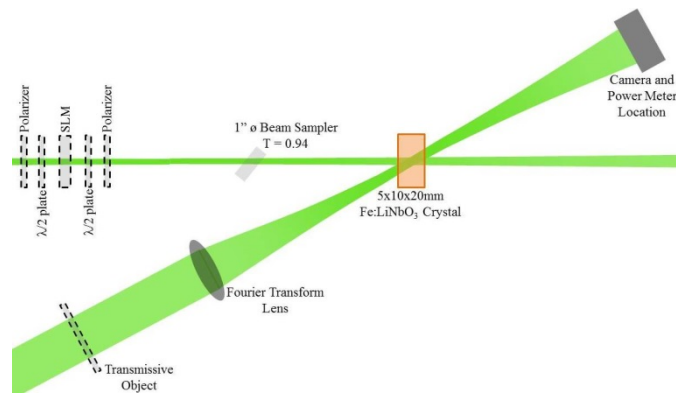


Fig. 13. Experimental setup for evaluating the cross-talk of single holograms.

The mode of the reference beam is controlled by setting the SLM to either a vertically split screen or a uniform screen. The split screen uses bit values of 0 and 157 to create a 0 to π phase step that bisects the incident Gaussian beam converting it to a HG 1,0 beam. The uniform screen uses a bit value of 157 over the entire SLM to make sure that the reference beam has the same

power inside the Fe:LiNbO₃ crystal. This is possible because of the “mostly phase” modulation of the SLM which has some amplitude modulation coupled to the phase. The profiles of the reference beams at the location of the Fe:LiNbO₃ crystal depicted in Fig. 13 are shown in Fig. 14.

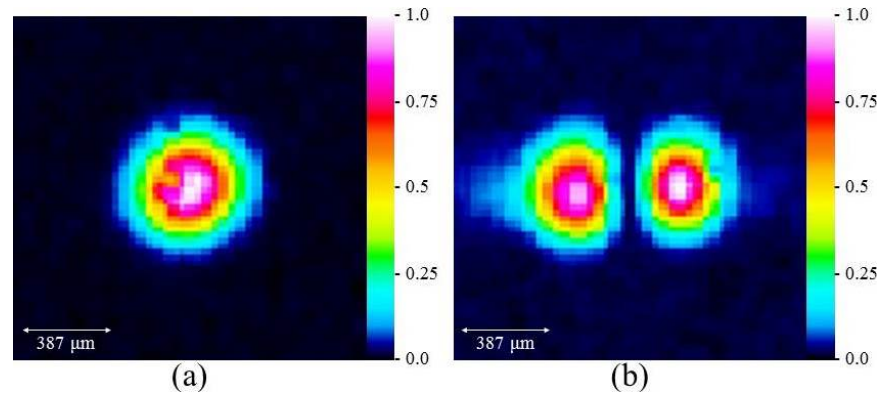


Fig. 14. Beam profiles for orthogonal reference beams: (a) the Gaussian reference beam and (b) the HG 1,0 reference beam at a location of recording material.

The largest number ‘2’ on a resolution bar target (USAF-1951 RES-1, Newport) is used as the object to be recorded. The original image is taken with the CMOS camera and the image is written once with a HG 0,0 reference beam and once at a separate location 1.5 mm apart with a HG 1,0 beam. The holograms are read out via both the HG 0,0 and 1,0 beam and the images are captured. The images can be seen in Fig. 15.

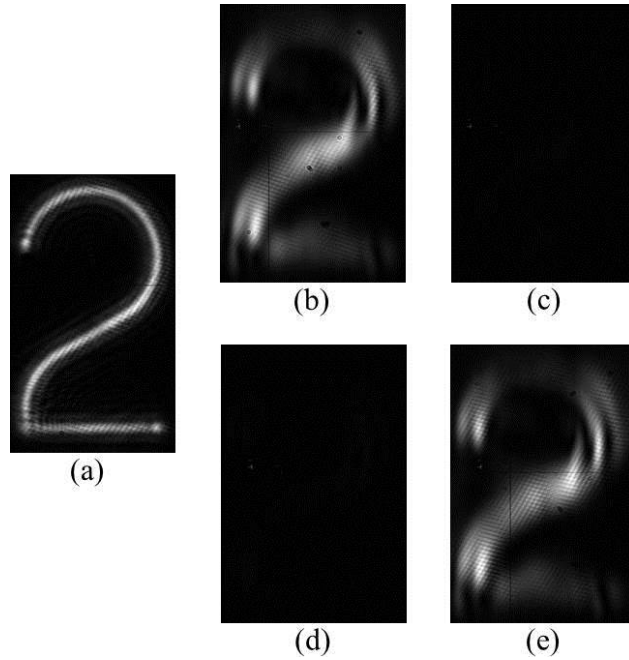


Fig. 15. Images for the mode multiplexing test: (a) original object recorded; (b) readout by an HG 0,0 beam of a hologram written with a HG 0,0 beam; (c) readout by an HG 1,0 beam of a hologram written with an HG 0,0 beam; (d) readout by an HG 0,0 beam of a hologram written with an HG 1,0 beam; (e) readout by an HG 1,0 beam of a hologram written with an HG 1,0 beam.

The diffraction efficiency of each hologram is recorded when illuminated with each reference beam. The hologram recorded with an HG 0,0 reference beam has a diffraction efficiency of 0.581% under HG 0,0 readout and 0.014% under HG 1,0 readout. Similarly, the hologram recorded with an HG 1,0 reference beam had diffraction efficiencies of 0.0066% and 0.393%. Taking the ratio of those diffraction efficiencies we find that recording with the HG 0,0 beam has a single page cross-talk of 2.5% and the HG 1,0 recording has a cross-talk of 1.7%.

Furthermore, this test was repeated with six other holograms at separate locations in the crystal for a total of eight holograms. Cross-talks were similar for HG 0,0 and 1,0 recording, so we report the mean of all eight cross-talks as 2.48% with a standard deviation of 1.17%.

4.1.2 *Image multiplexing with Hermite-Gaussian reference beams*

Using the experimental setup of Fig. 13, an image of the largest number ‘0’ on the USAF test chart is recorded using a HG 0,0 reference beam, and an image of the largest number ‘1’ is recorded at the same location using a HG 1,0 reference beam. The exposure times are adjusted to equalize the diffraction efficiencies of the two holograms. After recording, the two holograms are illuminated by each of the two reference beams, and the resulting images are captured.

Fig. 16 shows the captured images from the multiplexing experiment. This clearly demonstrates the low cross-talk of HG mode multiplexing as the ‘1’ does not show up in the ‘0’ image and vice versa. In this case we would expect cross-talks similar to those measured in Section 4.1.1.

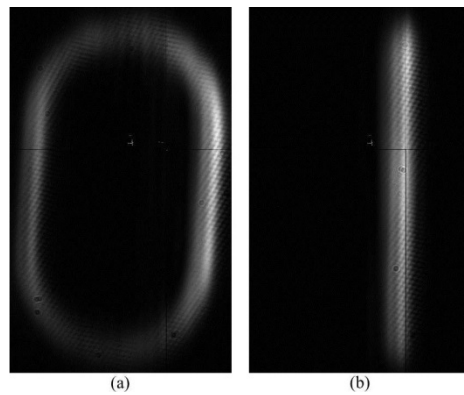


Fig. 16. Reconstructed images from HG mode multiplexing. (a) Image of the number ‘0’ reconstructed with the HG 0,0 beam. (b) Image of the number ‘1’ reconstructed with the HG 1,0 beam.

4.1.3 *Cavity enhanced writing with Hermite-Gaussian eigenmodes*

A setup similar to that of Fig. 8 in Section 3.2.2.1 is used, but the reference beam is the HG 1,0 generated by a Spatial Light Modulator (SLM) as in Fig. 13 of Section 4.1.1. The time evolutions of the diffraction efficiencies of a cavity and a non-cavity hologram recorded at adjacent locations separated by 1.5 mm are then compared by scaling the data to compensate for pseudo-

phase conjugate readout and convert the voltage data into actual diffraction efficiency values as in Section 3.2.2.2.

Taking the ratio of the non-cavity to cavity time constants we get the cavity enhanced write rate. For five trial pairs we get a Write Rate Enhancement (WRE) of 1.13 ± 0.03 . The cavity enhancement of irradiance was $G_F = 1.38 \pm 0.07$. With the theoretical WRE being $\sqrt{G_F}$, we expect a WRE of 1.18 ± 0.03 . Thus, we achieved 96% of the theoretical enhancement with the expected range of theory and result overlapping. This synchronicity proves that HG beams can be used in cavity enhanced recording. The results are summarized in Fig. 17 where the cavity enhanced diffraction efficiency evolves faster than normal writing, and the histogram insert shows that all five trials show enhancement.

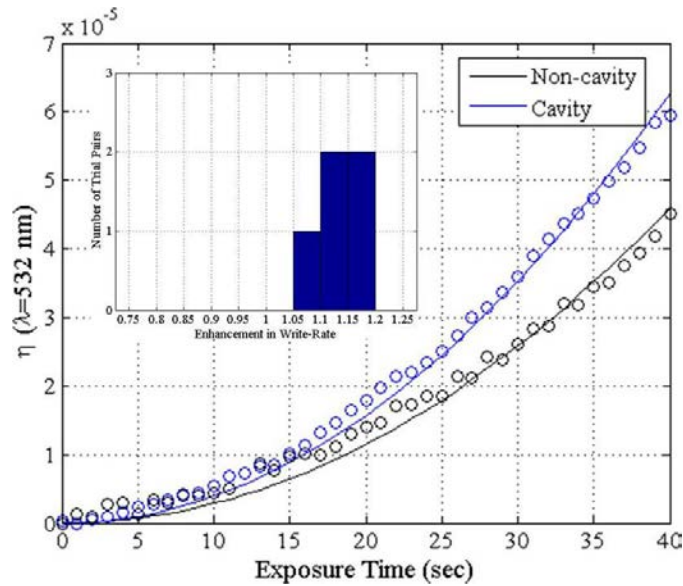


Fig. 17. Data and fitting curves for the best data set including a histogram of the write rate enhancements using a HG 1,0 reference beam. The non-cavity and cavity diffraction efficiency data have a time constants of 1.06×10^5 sec., and 0.909×10^5 sec., which yield a 1.17 enhancement in write data rate. The inset shows a histogram of write rate enhancements for the five trial pairs.

The single page cross-talk was also measured for three of these trials yielding an average cross-talk of $\sim 6.2\%$. This increase in cross-talk from cavity recording is likely due to poor mode

matching to the cavity. The 340 mm mode matching lens used is sufficient to allow cavity enhancement, but a better choice of mode matching lens would provide better mode purity in the cavity and higher enhancements.

4.1.4 Combined angular and mode multiplexing with cavity enhanced writing

Angular and mode multiplexing are combined while enhancing the write rate with a cavity on the reference arm. The experimental setup is similar to that of Section 4.1.3, except that the first polarizer, wave plate, and SLM have been replaced with a custom phase plate to convert the beam to an HG 1,0 beam. The Fe:LiNbO₃ crystal has also been remounted on a goniometer stage for angular multiplexing. The center of rotation of the goniometer is located at the crossing point of the reference and signal beams. Reconstructions are also observed by placing the CMOS camera where the transmissive object had been for pseudo phase conjugate readout.

Four holograms are multiplexed using 0° and 0.6° angles, and an HG 0,0 and an HG 1,0 reference beam. The 0.6° angular separation was chosen by monitoring the diffraction efficiency of a hologram written with a Gaussian reference beam: since Bragg side lobes are expected to be $\sim 1 \times 10^{-4}$ of the Bragg matched efficiency [39], we chose the separation by rotating the hologram to 1×10^{-2} of the Bragg matched efficiency, at 0.4°, and proceeded to the next increment on the goniometer stage, 0.6°. While this angle is likely still smaller than the first Bragg null, it provides angular cross-talks that are unmeasurable for single pages. Each hologram is written with a cavity enhanced reference beam with an average $G_F = 1.20$. First an image is recorded at 0° with an HG 0,0 beam, second an image is recorded at 0° with an HG 1,0 beam, third an image is recorded at 0.6° with an HG 1,0 beam, and fourth an image is recorded at 0.6° with an HG 0,0 beam. Each of the four images is reconstructed via pseudo-phase conjugate, cavity enhanced readout, and the results of the reconstructions are shown in Fig. 18.

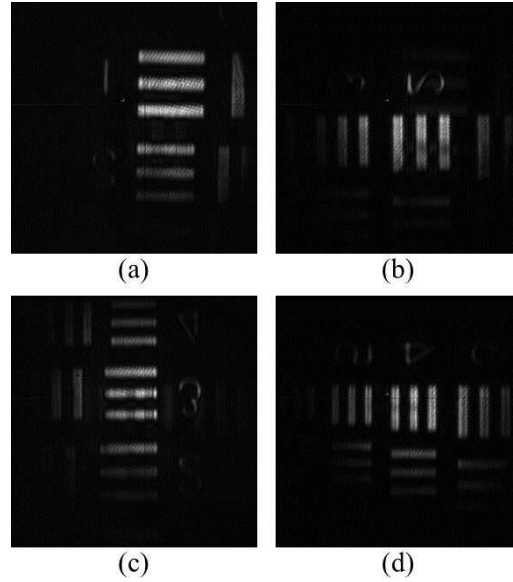


Fig. 18. Pseudo-phase conjugate reconstruction of images recorded (a) at 0° with HG 0,0, (b) at 0° with HG 1,0, (c) at 0.6° with HG 1,0, (d) at 0.6° with HG 0,0. $\sim 10\%$ Cross talk is visible in the reconstructions, and all holograms were written with an average enhancement of $G_F = 1.20$.

In Fig. 18, an average crosstalk of 10% is observed in the reconstructions, and is most visible in Fig. 18c, but careful control of cavity mode matching, and mode generation fidelity should remove this effect. This cross-talk is expected to be on the order of 6% as seen in Section 4.1.3, but the change of mode converter is likely responsible for this.

4.2 Mode-angular hybrid multiplexing discussion

Existing theory predicts zero cross-talk for plane wave signal holograms multiplexed using optical cavity eigenmodes [39], but we see cross-talks at $\sim 2.5\%$ in the single page trials of Section 4.1.1. This may be due to the cross-talk inherent in page base holography using image bearing object beams [44], but this cross-talk could also be due to several other factors: SLM phase error, SLM coupled amplitude modulation, Gaussian beam imperfections, and stray light.

The SLM has limited bit levels to choose from for setting the π phase shift, so some digitization error may be present in the split screen used to create the HG 1,0 beam. Concurrent to digitization error, the SLM used can only be made to operate in “mostly phase mode”, which

comes with some amplitude modulation coupled to the phase modulation [62,63]. The combination of these effects are likely responsible for the horizontal spread of the reference beam seen in the HG 1,0 beam profile of Fig. 14, which would decrease the purity of the beam and thus its orthogonality to the Gaussian beam. Similarly, any imperfections in the beam produced by our source would reduce orthogonality.

Cross-talk power readings may also have been influenced by stray light reflecting off of the many surfaces in the system. This is particularly likely as diffracted signals with matched reference and readout beams were on the order of 100 nW while the mismatched signals were on the order of 1 nW. The noise of the power meter was around 0.5 nW in the fully dark conditions that data was recorded, so SNR is on the order of 2 for measuring the diffraction efficiency in the mismatched case. This source of error is further supported by the lack of cross-talk seen in the images of Fig. 15. With all of these possible defects it is not surprising that we did not see zero cross-talk, and it is reasonable to expect that careful system design will reduce the cross-talk to more desirable levels.

For the recording of multiplexed images, Bashaw et. al include the effects of dephasing in broadband signal recording and show that orthogonal phase code multiplexing provides overall cross-talk to signal ratios which are a factor of two lower than those of angular multiplexing [44]. Such reduced cross-talk is appealing for reducing bit error rates and increasing recording density, but cavity eigenmode multiplexing cannot completely replace angular multiplexing for two reasons.

First, mode dimensions increase as the square root of the mode number, so the cavity diameter puts an upper limit on the number of modes that can be used [60]. Second, when using an FT recording geometry the mode profile of the reference beam affects the modulation transfer function in a manner similar to Gaussian apodization. If the reference mode contains a field null parallel to the signal and reference beam plane of incidence (e.g. HG 1,0), the reference beam will act like a high pass filter in recording. This further limits the available choices of cavity modes. Thus, reaching the industry goal of hundreds of multiplexed pages is impossible using only cavity eigenmodes.

Nonetheless, cavity enhanced mode multiplexing combined with angular multiplexing is feasible as seen in Section 4.1.4, and is an attractive way to increase data density. Adding mode multiplexing to an angular multiplexing scheme provides an additional DOF for system design increasing data densities toward the theoretical limit [7]. Currently, the number of multiplexed pages reported in literature is about 440 which is primarily limited by the angular extent of the reference beam scanning [64]. However, employing an HG 1,0 mode in the reference path in addition to the currently used HG 0,0 mode improves the number of multiplexing by a factor of 2. Although more area is needed due to the larger dimensions of higher order HG modes, the theoretical recording density still increases by about 1.33. Additionally, the reference path optics do not require substantial modifications. As seen in Fig. 14, the mode diameter along the horizontal direction increases by factor of 1.77 while the vertical dimension is unchanged. An ideal HG 10 has a 1/e field radius ~ 1.5 times larger than the HG 0,0 beam, so it is clear that the experimental beam is wider than it should be in theory. This may be a result of the phase error mentioned earlier or the fact that our FT geometry does not place the phase plate at the front focal plane or surface of the mode matching lens [61]. Experimentally, storage density increases by factor of $2/1.77 = 1.13$, but in theory increases by $2/1.5 = 1.33$. This seems like a small increase until we consider the trend as higher order modes are added, and the growth in beam size more closely matches the square root approximation [60]. The number of multiplexing increases as the maximum mode number plus one, and mode size increases like the square root of the maximum mode number, so the storage density will increase with the number of modes used as shown in Fig. 19, allowing for a factor of 2.1 storage density increase when five modes are used.

While mode multiplexing adds another DOF to HDSS design to increase data density, combining it with angular multiplexing raises the question of angular Bragg selectivity for mode multiplexed holograms. The effects of Gaussian apodization are known to reduce the height of the side lobes in angular multiplexing while increasing the angular width of the Bragg selectivity relative to plane wave reference beams [38,39]. The width of the Bragg selectivity decreases as the beam diameter increases, so we would expect higher order modes to create narrower Bragg

selectivities relative to Gaussian recording. Thus, overall, Bragg selectivity for higher order mode multiplexing does not negatively affect storage density, but further investigation is required before mode multiplexing can be implemented in commercial systems. Particularly, the optimum number of reference modes must be investigated while accounting for the tradeoffs in beam dimensions and Bragg selectivity, because higher order modes provide diminishing returns on storage density according to Fig. 19.

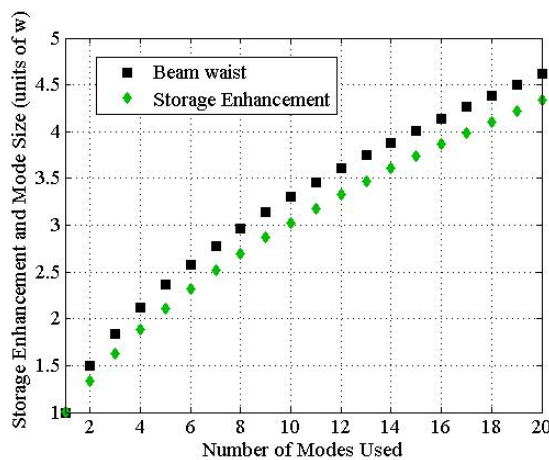


Fig. 19. Maximum mode size (units of Gaussian beam 1/e field radius) as a function of the number of modes used, and storage density enhancement as a function of number of modes used.

Bragg selectivity aside, orthogonal mode multiplexing has another advantage when paired with angular multiplexing. Angular multiplexed volume holographic data storage has an issue with beam fanning, which can hinder the use of pseudo-phase conjugate readout when present in the reference arm, but the use of orthogonal reference beams causes the total beam fanning effect to be divided over the all of the reference beams used. Since the reference beams are orthogonal, the beam fanning caused by the self-interference of the reference beams is also matched to the reference beam that created those patterns. Thus beam fanning caused by an HG 1,0 reference is separate from fanning caused by an HG 0,0 reference. This orthogonality of fanning means that fanning of the reference beam should be reduced by a factor equal to or greater than the number of reference beams used.

4.3 Summary of cavity enhanced mode-angular multiplexing

Holograms written with HG modes are seen to demonstrate cross-talks on the order of 2.5%, and multiplexing with an HG 0,0 and HG 1,0 mode is demonstrated with no visible cross-talk in the reconstructed images. Images are also successfully recorded with a cavity enhanced HG 1,0 reference arm, and 96% of the expected write-rate enhancement of 1.18. Finally, all three experiments are combined to record four images in the same volume using angular multiplexing, orthogonal mode multiplexing, and cavity enhanced recording. The combined technique yields a write-rate enhancement of 1.1 and a cross-talk of ~10%.

Cross-talks and cavity enhancements can be improved by careful system design, so that combining mode multiplexing with angular multiplexing, and cavity enhanced recording is functionally limited by the increasing diameter of higher order modes. The diminishing returns from increasing the number of modes require the use of five modes to improve storage densities by a factor of two. Thus, such a cavity enhanced hybrid multiplexing scheme can provide substantial increases in HDSS storage densities.

5 Summary of contributions and suggestions on technology transfer towards commercialization

While the potential of cavity enhanced readout of holograms is already well understood [36,37], cavity enhanced recording was only proposed in passing. Consequently, the theory outlined in Section 3.1 is completely novel in addressing the relation of the cavity irradiance enhancement factor, G_F , to the enhancement of recording speeds. Equation (34) describes enhancement in write rate as a function of the splitting ratio provided only one data bearing hologram is formed, and this is helpful in understanding the basic potential of cavity enhanced HDSS for the first time. This theory is also verified for the first time in Section 3.2 where the result agrees to within a 3% error.

Leaving the analysis for a single data bearing grating, Section 0 includes the new topic of how the extra gratings of standing wave cavity enhanced recording affects recording speeds while maintaining a dynamic range consumption equivalent to normal recording. Eq. (50) provides an analytical form for the total enhancement in write rate assuming that the splitting ratio is chosen to maximize the diffraction efficiency yield. A similar recording technique was suggested by Cao et. al to increase the uniformity of the exposure of the recording medium [40], but they neither used cavities nor addressed the issue of the existence of the extra grating formed with a reverse propagating reference beam. The combined theory and experiments of Section 3 provide a new way to increase write data rates or system energy needs in HDSS without the added cost of developing higher sensitivity recording materials.

While this technique is compatible with current HDSS systems, some changes will need to be made to accommodate the cavity in the reference beam path. To begin, the reference beam in the monocular architecture is scanned over the required multiplexing angles with the hologram volume at the center of rotation. In order to accommodate this behavior the spherical mirror(s) of the cavity must be large enough diameter to accommodate the reference beam movement and placed so that the reference beam rotates about the mirrors center of curvature. Larger radii of curvature of the cavity mirrors and cavity lengths increase the size of the resonant modes, so the

cavity parameters must be chosen to match the desired reference beam size. Aberrations from the read-write lens will also have an effect on the mode purity as the reference beam is scanned over the lens, so lens optimization may be needed to reduce gain losses due to poor mode matching. Finally, as mentioned in Section 3.3.1, the cavity will require cavity lengths to be stable to accuracies on the order of $\lambda/100$, so some manner of fast stabilization is required [65,66].

Adding orthogonal mode multiplexing to cavity enhanced angular multiplexing, we find that the idea was originally proposed and theoretically analyzed by Tian [39], but never tested experimentally. Mode multiplexing of micro-holograms without cavity enhancement has also been proposed and tested [41,43], but Section 4.1 demonstrates the first cavity enhanced volume holographic multiplexing using cavity modes. In addition to the new experiments, Section 4.2 Fig. 19 shows a first order projection of the storage density increase expected by using HG reference multiplexing combined with angular multiplexing, which expands upon the four mode density increase described by Mikami [41].

Fortunately, the only complication that mode multiplexing adds to cavity enhanced HDSS is a phase-only SLM which must be FT'ed onto the recoding medium. The effect of this modification would likely use existing read/write lens as the FT lens, so integrating the new SLM would be the primary challenge.

6 Conclusions and future work

In this time when massive internet bandwidths make remote data storage a reality, storage providers must find ways to store the worlds data as economically as possible without compromising on data transfer rates or archive life span. While SSD and magnetic technologies are ideal solutions for frequently accessed and changed data, the stable or immutable data like photos, music, videos, etc. need to be kept on cheaper more stable media to ensure the longevity of the information. Since the creation of the Compact Disc (CD) optical data storage has been the preferred method of long term data storage, but resolution limits have caused the development of such bit based technologies as DVD, Blu-ray, and AD to taper off. Fortunately, after nearly 70 years of research, the technology needed to make HDSS commercially viable has allowed HDSS to develop rapidly into the next generation of optical data storage technology.

As this new technology comes to market researchers continue to refine existing techniques and develop new ones to reach the storage limit that van Heerden described at the beginning of HDSS development [7]. Our contributions to the growth of HDSS directly impact the recording speed or energy efficiency of HDSS, and provide increased data density.

Our first such contribution provides an improved power usage during data recording. By recycling the light of the reference beam with a resonant optical cavity, we have demonstrated that HDSS can be made more energy efficient, providing a lower total cost of ownership, or made faster in recording, providing higher data rates. Experimentally, we have achieved 98% of our theoretical enhancement in write rate with a factor of 1.19 improvement. However, this proof of concept is just a starting point. Assuming reasonable system parameters, and using only one of the gratings created by standing wave recording, write-rates can be increased by a factor as high as 1.6. Including the extra gratings formed by standing wave writing, the experimental write rate can be improved from a factor 1.22 to a factor of 1.69. Experimental results aside, our development of cavity enhanced recording theory provides future HDSS developers with the tools to adapt our work to their systems.

In addition to gains in write data rates and system energy efficiency, cavity enhanced writing supports cavity eigenmodes. These eigenmodes provide a set of orthogonal functions to enable orthogonal phase code multiplexing while enjoying benefit of cavity enhancement. We have demonstrated the low cross-talk of this multiplexing technique ($\sim 2.5\%$), and confirmed that cavity enhanced recording is still achievable with these modes at an average factor of 1.13 write rate enhancement, which can be increased by careful system design. Combining mode multiplexing with angular multiplexing was also demonstrated, and we expect to be able to more than double HDSS storage densities by combining 5 modes with compatible multiplexing techniques.

The logical progression of this work would implement a cavity enhanced signal arm in the FT or near FT image recording used in page based storage. The plane wave theory used here would need to be replaced with an expansion in the cavity eigenmodes. The arbitrary Guoy phase shift of a given cavity limits the modes which can be coupled into, but a π phase shift would allow for propagation of all modes. Thus any image could be coupled into a π Guoy phase shift cavity, such as a concentric standing wave cavity, as an expansion in Laguerre or Hermite Gaussian beams due to these polynomials forming complete set of orthogonal basis functions [49]. Thus, the only challenge in implementing an image carrying, cavity enhanced, signal beam would be integrating the resonator with the Fourier transform recording geometry. Unfortunately, while such π Guoy phase shift cavities would allow for all spatial modes to propagate simultaneously, the mode diameter collapses to zero, so such cavities are conditionally stable. Similar to planar resonator cavities, these π phase shift cavities do not have eigenmodes, and their enhancement will be limited by diffraction losses.

Further analysis and testing of such image bearing π phase shift cavities may be profitable, but using an incomplete set of eigenmodes may also provide a means to creating cavity enhanced image bearing signal beams. For instance, a $\pi/3$ phase shift cavity would allow for the highest density of allowable eigenmodes within a certain maximum mode index. Naturally, this incomplete set of orthogonal basis functions will result in an unusual Modulation Transfer Function. Such limited functionality may be sufficient for HDSS as is, or it may require certain

restrictions on the input signal beam. Such issues are of interest for the future of HDSS and its cavity enhanced techniques.

Appendix A: Publications

1. B. E. Miller and Y. Takashima, "Formalization and experimental evaluation of cavity-enhanced holographic readout," Proc. SPIE **920104**, (2014) [doi:10.1117/12.2061448].
2. B. E. Miller and Y. Takashima, "Enhancement of data rates by single and double cavity holographic recording," Proc. SPIE **95870G**, (2015) [doi:10.1117/12.2187253].
3. B. E. Miller and Y. Takashima, "Cavity techniques for holographic data storage recording," Opt. Express **24**, 6300 (2016) [doi:10.1364/OE.24.006300].
4. B. E. Miller and Y. Takashima, "Cavity enhanced image recording for holographic data storage," Proc. SPIE **9959-3**, (2016) [doi:10.1117/12.2237078].
5. B. E. Miller and Y. Takashima, "Enabling energy-efficient holographic optical storage for cold data," SPIE Newsroom (2016) [doi:10.1117/2.1201610.006728].
6. B. E. Miller and Y. Takashima, "Cavity enhanced image recording for holographic data storage," Proc. SPIE **995903**, (2016) [doi:10.1117/12.2237078].
7. B. E. Miller and Y. Takashima, "Cavity-enhanced eigenmode and angular hybrid multiplexing in holographic data storage systems," Submitt. Opt. Express (2016).

Appendix B: MATLAB code for determining recording time constants

The following code was used in the data analysis of Sections 3.2.1.2, 3.2.2.2, and 4.1.3.

1 Main fitting code

```
% Title: DataProc_02152016.m
% Author: Bo Miller
% Company: Universtiy of Arizona, College of Optical Sciences, Takashima
% Group
% Date: 02/15/2016
% Description: This script imports the data from .csv files generated by a
% Fluke Hydra Data Logger for trials dating from 07/06/2015 to 07/16/2015.
% It windows the data with a maximum exposure time of t_max, normalizes
% each pair based on the non-cavity data, and fits a
% sin^2(n_max(1-exp(-t/tau)). It then computes the enhancement in write rate
% by comparing the time constants fo the trial pairs.

clear all;
close all;
clc;
tic

%Initialize the fit coefficient matrix
numtrials = 11; % the number of trial pairs to process
p = zeros(2*numtrials,2); % matrix of the non-cavity fitting coefficients
foG_F = zeros(numtrials,1); % vector of write rate enhancement values
t_max = 80; % maximum exposure time to inlcued in the analysis
t = [0:1:t_max]; % ideal exposure time vector
tauguess = 1e5; % max index change and time constant guessed for fitting
Aguess = 7;

% Conversion factor from v/uW to diffraciton efficinecy in 532nm. Derived
% from data collected from 8/22 to 8/29/2015.
con = 1.05e-3;

% Import the Non-cavity and Cavity data sets and place them in cell arrays.
%-----

% Load the raw data from datacells file
load('datacells');

%%%%%%%%%%%%%%%%%%%%%%%%%%%%%%%%%%%%%%%%%%%%%%%%%%%%%%%%%%%%%%%%%%%%%%%%
%%%%%%%%Uncomment this block to reimport the raw data from the files%%%%%%%%
%%%%%%%%%%%%%%%%%%%%%%%%%%%%%%%%%%%%%%%%%%%%%%%%%%%%%%%%%%%%%%%%%%%%%%%%
```

```

% etacell = cell(2*numtrials,3,1);
% tcell = etacell;
%
% %Trial #1
% etacell{1,1} = xlsread('non_0p5x0p55y_07062015.xlsx','D6:D278'); %non-
cavity diffraction efficiency data
% tcell{1,1} = xlsread('non_0p5x0p55y_07062015.xlsx','A6:A278'); %time axis
%
% etacell{2,1} =
xlsread('cavity_lowtune_0p5x0p519y_07062015.xlsx','D6:D278'); %cavity
diffraction efficiency data
% tcell{2,1} = xlsread('cavity_lowtune_0p5x0p519y_07062015.xlsx','A6:A278');
%time axis
%
% %Trial #2
% etacell{3,1} = xlsread('non_0p5x0p488y_07062015.xlsx','D6:D278'); %non-
cavity diffraction efficiency data
% tcell{3,1} = xlsread('non_0p5x0p488y_07062015.xlsx','A6:A278'); %time axis
%
% etacell{4,1} =
xlsread('cavity_lowtune_0p5x0p457y_07062015.xlsx','D6:D278'); %cavity
diffraction efficiency data
% tcell{4,1} = xlsread('cavity_lowtune_0p5x0p457y_07062015.xlsx','A6:A278');
%time axis
%
% %Trial #3
% etacell{5,1} = xlsread('non_0p5x0p426y_07102015.xlsx','D6:D300'); %non-
cavity diffraction efficiency data
% tcell{5,1} = xlsread('non_0p5x0p426y_07102015.xlsx','A6:A300'); %time axis
%
% etacell{6,1} =
xlsread('cavity_lowtune_0p5x0p395y_07102015.xlsx','D6:D300'); %cavity
diffraction efficiency data
% tcell{6,1} = xlsread('cavity_lowtune_0p5x0p395y_07102015.xlsx','A6:A300');
%time axis
%
% %Trial #4
% etacell{7,1} = xlsread('non_0p5x0p364y_07102015.xlsx','D6:D300'); %non-
cavity diffraction efficiency data
% tcell{7,1} = xlsread('non_0p5x0p364y_07102015.xlsx','A6:A300'); %time axis
%
% etacell{8,1} =
xlsread('cavity_lowtune_0p5x0p333y_07102015.xlsx','D6:D300'); %cavity
diffraction efficiency data
% tcell{8,1} = xlsread('cavity_lowtune_0p5x0p333y_07102015.xlsx','A6:A300');
%time axis
%
% %Trial #5
% etacell{9,1} = xlsread('non_0p5x0p271y_07132015.xlsx','D6:D300'); %non-
cavity diffraction efficiency data

```

```

% tcell{9,1} = xlsread('non_0p5x0p271y_07132015.xlsx','A6:A300'); %time axis
%
% etacell{10,1} =
xlsread('cavity_lowtune_0p5x0p24y_07142015.xlsx','D6:D300'); %cavity
diffraction efficiency data
% tcell{10,1} = xlsread('cavity_lowtune_0p5x0p24y_07142015.xlsx','A6:A300');
%time axis
%
% %Trial #6
% etacell{11,1} = xlsread('non_0p5x0p209y_07142015.xlsx','D6:D300'); %non-
cavity diffraction efficiency data
% tcell{11,1} = xlsread('non_0p5x0p209y_07142015.xlsx','A6:A300'); %time axis
%
% etacell{12,1} =
xlsread('cavity_lowtune_0p5x0p178y_07142015.xlsx','D6:D300'); %cavity
diffraction efficiency data
% tcell{12,1} = xlsread('cavity_lowtune_0p5x0p178y_07142015.xlsx','A6:A300');
%time axis
%
% %Trial #7
% etacell{13,1} = xlsread('non_0p44x0p55y_07142015.xlsx','D6:D300'); %non-
cavity diffraction efficiency data
% tcell{13,1} = xlsread('non_0p44x0p55y_07142015.xlsx','A6:A300'); %time axis
%
% etacell{14,1} =
xlsread('cavity_lowtune_0p44x0p519y_07142015.xlsx','D6:D300'); %cavity
diffraction efficiency data
% tcell{14,1} =
xlsread('cavity_lowtune_0p44x0p519y_07142015.xlsx','A6:A300'); %time axis
%
% %Trial #8
% etacell{15,1} = xlsread('non_0p44x0p488y_07152015.xlsx','D6:D300'); %non-
cavity diffraction efficiency data
% tcell{15,1} = xlsread('non_0p44x0p488y_07152015.xlsx','A6:A300'); %time
axis
%
% etacell{16,1} =
xlsread('cavity_lowtune_0p44x0p457y_07152015.xlsx','D6:D300'); %cavity
diffraction efficiency data
% tcell{16,1} =
xlsread('cavity_lowtune_0p44x0p457y_07152015.xlsx','A6:A300'); %time axis
%
% %Trial #9
% etacell{17,1} = xlsread('non_0p44x0p426y_07152015.xlsx','D6:D300'); %non-
cavity diffraction efficiency data
% tcell{17,1} = xlsread('non_0p44x0p426y_07152015.xlsx','A6:A300'); %time
axis
%

```

```

% etacell{18,1} =
xlsread('cavity_lowtune_0p44x0p395y_07152015.xlsx','D6:D300'); %cavity
diffraction efficiency data
% tcell{18,1} =
xlsread('cavity_lowtune_0p44x0p395y_07152015.xlsx','A6:A300'); %time axis
%
% %Trial #10
% etacell{19,1} = xlsread('non_0p44x0p302y_07162015.xlsx','D6:D300'); %non-
cavity diffraction efficiency data
% tcell{19,1} = xlsread('non_0p44x0p302y_07162015.xlsx','A6:A300'); %time
axis
%
% etacell{20,1} =
xlsread('cavity_lowtune_0p44x0p333y_07162015.xlsx','D6:D300'); %cavity
diffraction efficiency data
% tcell{20,1} =
xlsread('cavity_lowtune_0p44x0p333y_07162015.xlsx','A6:A300'); %time axis
%
% %Trial #11
% etacell{21,1} = xlsread('non_0p44x0p24y_07162015.xlsx','D6:D300'); %non-
cavity diffraction efficiency data
% tcell{21,1} = xlsread('non_0p44x0p24y_07162015.xlsx','A6:A300'); %time axis
%
% etacell{22,1} =
xlsread('cavity_lowtune_0p44x0p271y_07162015.xlsx','D6:D300'); %cavity
diffraction efficiency data
% tcell{22,1} =
xlsread('cavity_lowtune_0p44x0p271y_07162015.xlsx','A6:A300'); %time axis
%
% % Save the cell arrays containing the data
% save('datacells','etacell','tcell');
%%%%%%%%%%%%%%%%%%%%%%%%%%%%%%%%%%%%%%%%%%%%%%%%%%%%%%%%%%%%%%%%%%%%%%%%

% Convert the data sets to diffraction efficiency in 532nm.
etacell(:,1) = cellfun(@(x) x*con,etacell(:,1),'un',0);

% Shift data sets by the 30 second pre-exposure and add a zero value at
% time 0.
tcell(:,2) = cellfun(@(x) [0 (0:1:x(end))+30],tcell(:,1),'un',0);
etacell(:,2) = cellfun(@(x) [0 x'],etacell(:,1),'un',0);

% Window the data with t_max
tcell(:,3) = cellfun(@(x) x(x<=t_max),tcell(:,2),'un',0);
etacell(:,3) = cellfun(@(x,y) x(1:length(y)),etacell(:,2),tcell(:,3),'un',0);

% Fit the cavity and non-cavity data
%-----

```

```

options = optimset('Tolx',1e-20,'TolFun',1e-20); %fitting options to force
convergence

for k=1:2*numtrials
    p(k,:) = [Aguess
lsqnonlin(@residues_EtaSine,tauguess,[],[],options,tcell{k,3},etacell{k,3},Ag
uess)];
end;

% Compute the enhancement values for the trial pairs
foG_F = p(1:2:end,2)./p(2:2:end,2)
mean(foG_F)
std(foG_F)
mean(foG_F([1:3 6 10]))
std(foG_F([1:3 6 10]))

% Evaluate the fits of the data
%-----
fitmat = zeros(2*numtrials,length(t));
for k = 1:(2*numtrials)
    fitmat(k,:) = residues_EtaSine(p(k,2),t,0,p(k,1));
end

% Plot the raw data and the fits for the values of G_F
%-----
for k = 1:2:(2*numtrials)
    figure((k+1)/2);
    hold on;
    plot(t,fitmat(k,:), 'k');
    plot(t,fitmat(k+1,:), 'b');
    plot(tcell{k,3},etacell{k,3}, 'ok');
    plot(tcell{k+1,3},etacell{k+1,3}, 'ob');
    set(gca, 'Xlim',[0 t_max], 'Ylim',[0 1e-3]);
    set(gca, 'FontName', 'Times New Roman');
    set(gca, 'FontSize',12, 'Xgrid', 'on', 'Ygrid', 'on', 'Ytick', (0:1e-4:1e-3));
    xlabel('Exposure Time (sec)', 'FontSize', 14);
    ylabel('\eta (\lambda=532 nm)', 'FontSize',14);
    title(['\lambda=532nm, \eta vs. Time, f(G_F)='
num2str(foG_F((k+1)/2))], 'FontSize',14);
    legend('Non-cavity', 'Cavity');
    hold off;
end

% Plot all of the raw data on a single plot
figure(12);
hold on;
for k = 1:2:(2*numtrials)
    plot(tcell{k,3},etacell{k,3}, 'ok', 'MarkerFaceColor', 'k');
    plot(tcell{k+1,3},etacell{k+1,3}, 'squareb', 'MarkerFaceColor', 'b');

```

```

end;
set(gca, 'Xlim', [30 t_max], 'Ylim', [0.5e-4 6.5e-4]);
set(gca, 'FontSize', 12, 'Xgrid', 'on', 'Ygrid', 'on', 'Ytick', (0:0.5e-4:6.5e-4));
xlabel('Exposure Time (sec)', 'FontSize', 14);
ylabel('\eta (\lambda=532 nm)', 'FontSize', 14);
title('\lambda=532nm, \eta vs. Time', 'FontSize', 14);
legend('Non-cavity', 'Cavity');
hold off;

% Normalize the raw data by the maximum non-cavity diffraction efficiency
% and plot the results on a single plot.
for k = 1:2:(2*numtrials)
    etacell{k,4} = etacell{k,3}./max(etacell{k,3});
    etacell{k+1,4} = etacell{k+1,3}./max(etacell{k,3});
end;

tcell(:,4)=tcell(:,3);

% Plot exposure time vs. normalized diffraction efficiency
figure(13);
hold on;
handle = zeros(1,3);
for k = 1:2:(2*numtrials)
    handle(1)=plot(etacell{k,4},tcell{k,4}, 'ok', 'LineWidth', 2);
end
for k = [4 5 7:9 11]*2
    handle(2)=plot(etacell{k,4},tcell{k,4}, '+b', 'LineWidth', 2);
end;
for k = [1:3 6 10]*2
    handle(3)=plot(etacell{k,4},tcell{k,4}, '+', 'color', [0 0.75
0], 'LineWidth', 2);
end;
legend(handle, 'Non-Cavity', 'Failed Cavity', 'Enhanced Cavity');
set(gca, 'Xlim', [0.1 1.5], 'Ylim', [30 t_max]);
set(gca, 'FontSize', 12, 'Xgrid', 'on', 'Ygrid', 'on', 'Ytick', (0:5:t_max));
set(gca, 'FontName', 'Times New Roman');
set(gca, 'Xtick', (0:0.1:1.5));
xlabel('Normalized \eta', 'FontSize', 12);
ylabel('Exposure Time (sec)', 'FontSize', 12);
title('Exposure Time vs. Normalized \eta', 'FontSize', 12);
hold off;

% Create a histogram of the diffraction efficiency enhancements
dx = 0.05;
XLim = [(1+dx/2)-floor((1+dx/2-0.7)/dx)*dx (1+dx/2)+floor((1.3-1-
dx/2)/dx)*dx];
fsize = 14;
figure(14);
hold on;
hist(foG_F, XLim(1):dx:XLim(end));

```

```

[nel,cent] = hist(foG_F,XLim(1):dx:XLim(end));
set(gca,'XLim',XLim,'YLim',[0 3]);
set(gca,'FontName','Times New Roman');
set(gca,'FontSize',fsize,'Xgrid','on','XTick',[cent cent(end)+dx]-
dx/2,'Ygrid','on');
set(gca,'Ytick',0:3);
xlabel('Enhancement in Write-Rate','FontSize',fsize);
ylabel('Number of Trial Pairs','FontSize',fsize);
title('Histogram of Write-Rate Enhancement','FontSize',fsize);
hold off;
toc

```

1.1 MATLAB residues function

The following code is a MATLAB function called by the main code of Appendix B Section 1.

```

function diffs = residues_EtaSine(tau,t,f,A)

% Name: residues_fermi.m
% Author: Bo Miller
% Date: 11/13/2015
% Company: Takashima Group, Universtiy of Arizona, College of Optical
% Sciences
% Description: This function is called by lsqnonlin. It computes the
% residuals for a function of the form  $\sin^2(A*(1-\exp(t/\tau)))$ .

% A=pars(1);
%
% tau=pars(2);

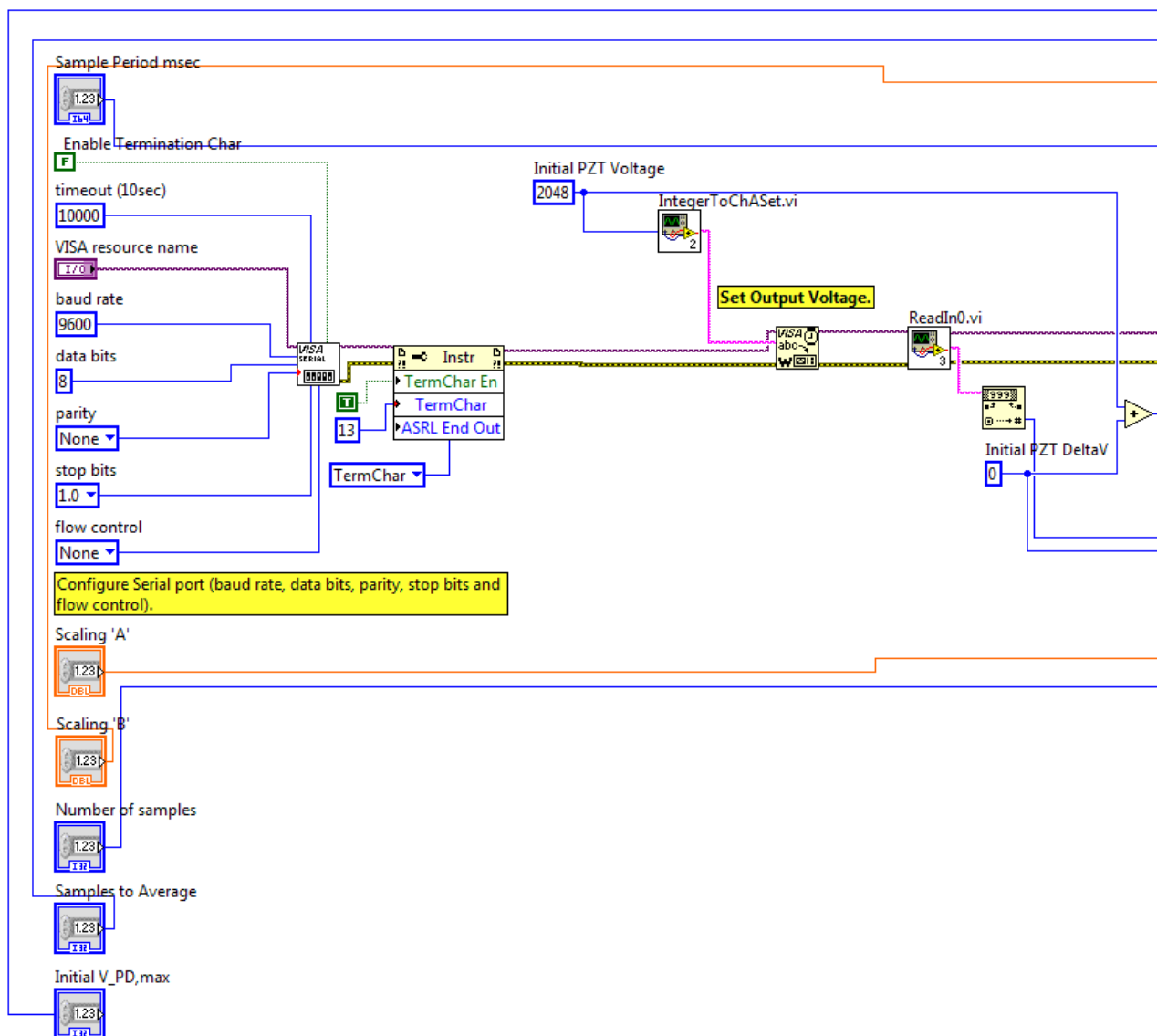
diffs = sin(A*(1-exp(t/tau))).^2-f; %

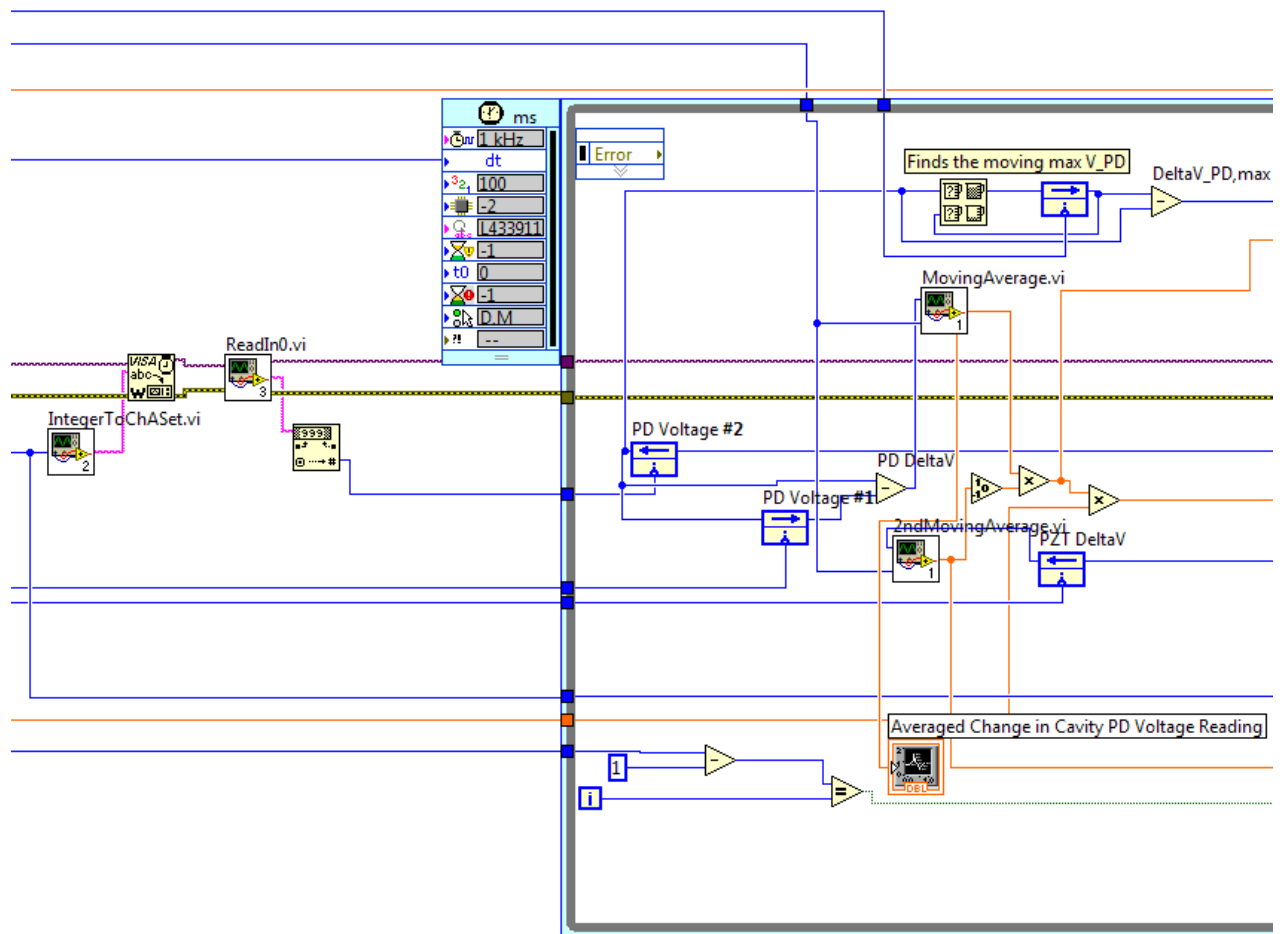
```

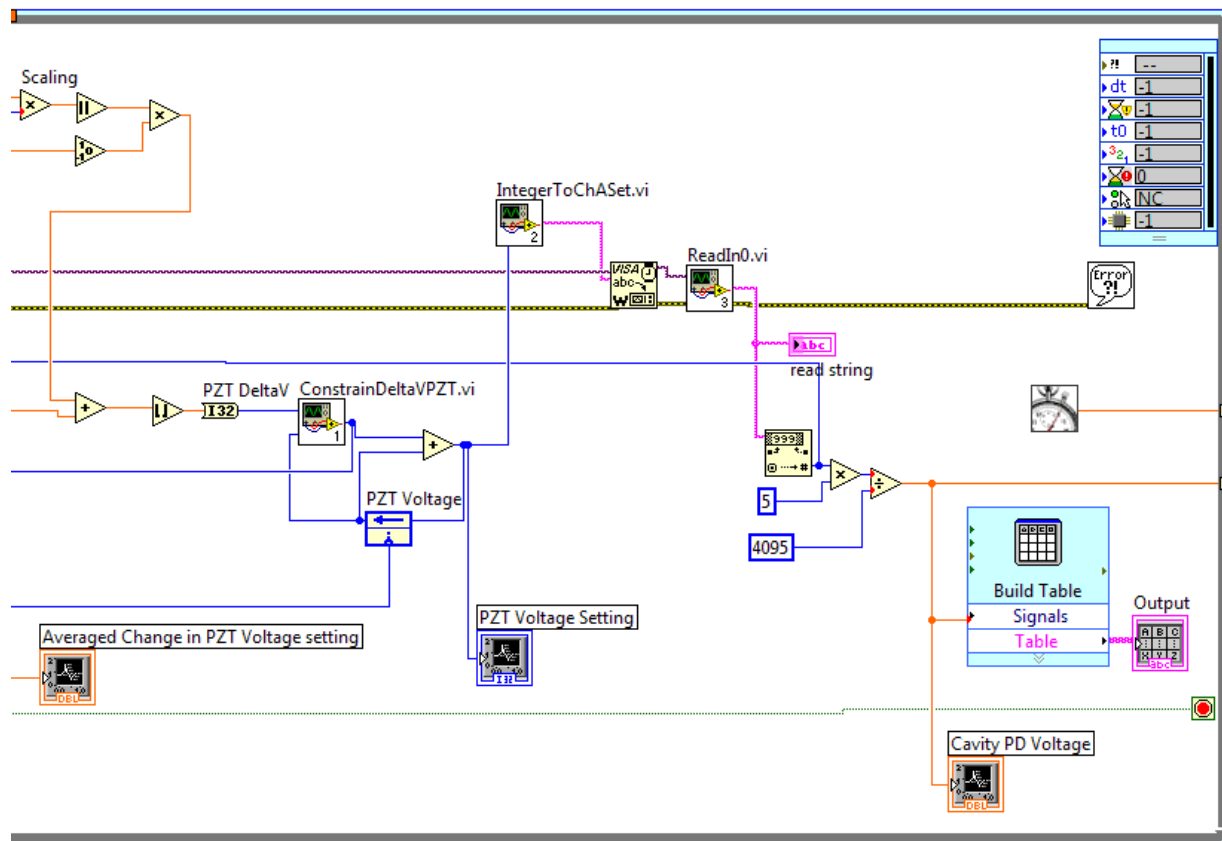
Appendix C: LabVIEW code for proportional gain feedback loop

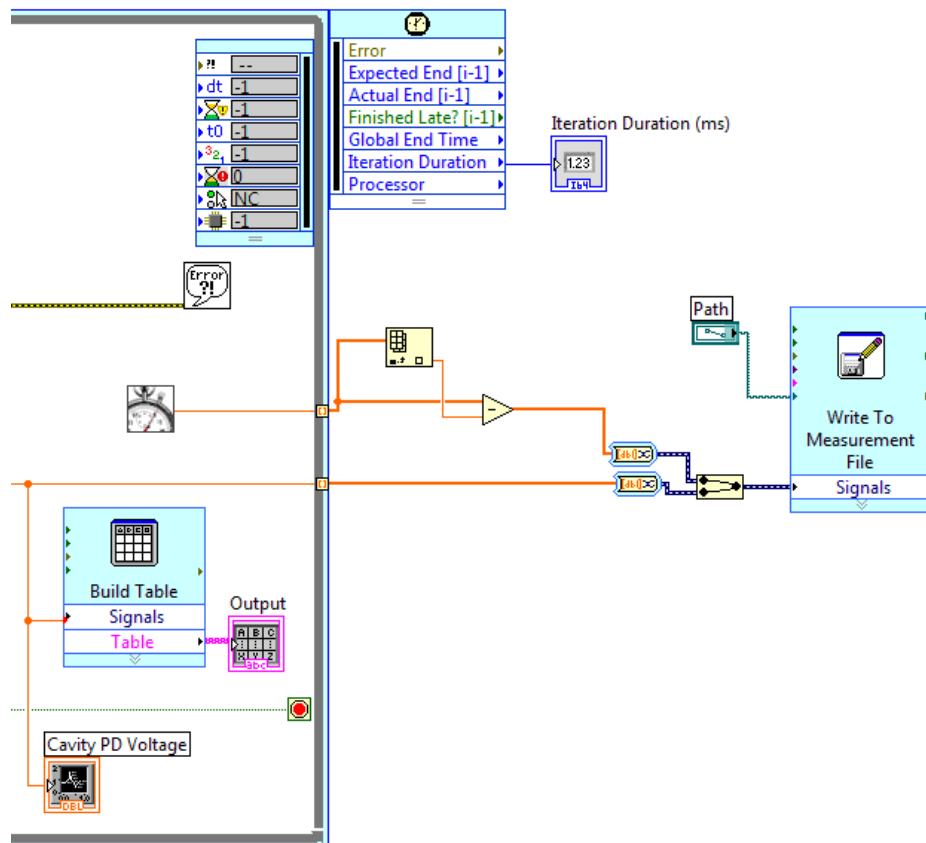
This appendix contains LabVIEW block diagrams which run the proportional gain feedback loop for controlling the cavity length as used in Sections 3.2.2 and 4.1.3.

1 Main block diagram



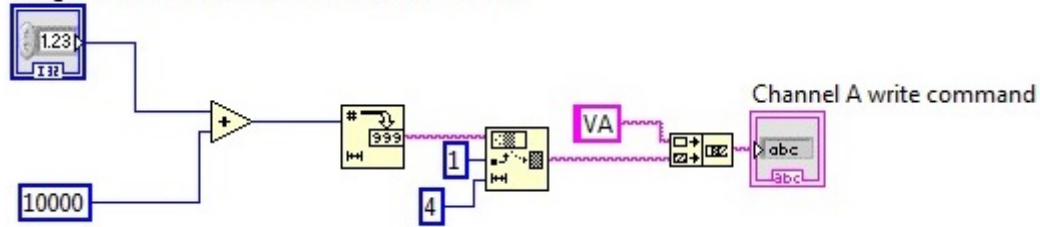




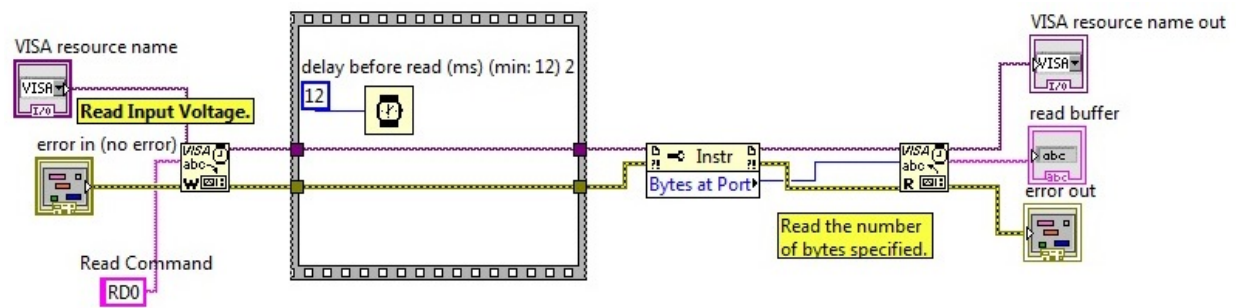


1.1 IntToChASet.vi sub-vi

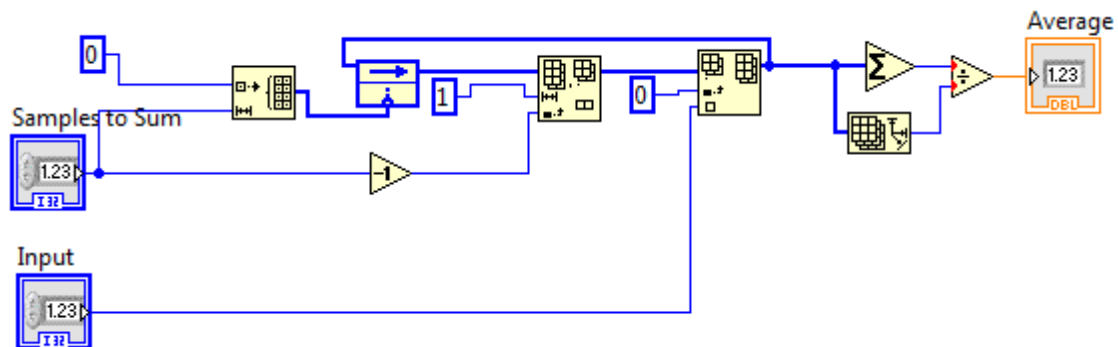
Integer to convert to Channel A write command



1.2 ReadIn0.vi sub-vi



1.3 MovingAverage.vi sub-vi



References

1. M. R. Ayres, K. Anderson, F. Askham, B. Sissom, and A. C. Urness, "Holographic data storage at 2+ Tbit/in²," Proc. SPIE **9386**, 93860G (2015) [doi:10.1117/12.2080156].
2. M. Hosaka, T. Ishii, A. Tanaka, S. Koga, and T. Hoshizawa, "1 Tbit/inch² Recording in Angular-Multiplexing Holographic Memory with Constant Signal-to-Scatter Ratio Schedule," Jpn. J. Appl. Phys. **52**, 09LD01 (2013) [doi:10.7567/JJAP.52.09LD01].
3. D. Clark, "Startups Dash Into Hot Data-Storage Sector," <http://www.wsj.com/articles/startups-dash-into-hot-data-storage-sector-1441409495>.
4. "White Paper: Archival Disc Technology," http://panasonic.net/avc/archiver/pdf/E_WhitePaper_ArchivalDisc_Ver100.pdf.
5. R. R. McLeod, A. J. Daiber, M. E. McDonald, T. L. Robertson, T. Slagle, S. L. Sochava, and L. Hesselink, "Microholographic multilayer optical disk data storage," Appl. Opt. **44**, 3197 (2005) [doi:10.1364/AO.44.003197].
6. I. Ichimura, K. Saito, T. Yamasaki, and K. Osato, "Proposal for a multilayer read-only-memory optical disk structure," Appl. Opt. **45**, 1794 (2006) [doi:10.1364/AO.45.001794].
7. P. J. van Heerden, "Theory of Optical Information Storage in Solids," Appl. Opt. **2**, 393 (1963) [doi:10.1364/AO.2.000393].
8. G. Barbastathis and D. Psaltis, "Volume Holographic Multiplexing Methods," in *Holographic Data Storage*, D. H. J. Coufal, P. D. Psaltis, and P. G. T. Sincerbos, eds., Springer Series in Optical Sciences No. 76 (Springer Berlin Heidelberg, 2000), pp. 21, 57–59.
9. K. Anderson, M. Ayres, F. Askham, and B. Sissom, "Holographic Data Storage: Science Fiction or Science Fact," Proc. SPIE **9201**, 920102 (2014) [doi:10.1117/12.2061402].
10. F. H. Mok, "Angle-multiplexed storage of 5000 holograms in lithium niobate," Opt. Lett. **18**, 915–917 (1993) [doi:10.1364/OL.18.000915].
11. L. d'Auria, J. P. Huignard, C. Slezak, and E. Spitz, "Experimental Holographic Read-Write Memory Using 3-D Storage," Appl. Opt. **13**, 808–818 (1974) [doi:10.1364/AO.13.000808].

12. N. Kinoshita, T. Muroi, N. Ishii, K. Kamijo, and N. Shimidzu, "Control of Angular Intervals for Angle-Multiplexed Holographic Memory," *Jpn. J. Appl. Phys.* **48**, (2009) [doi:10.1143/JJAP.48.03A029].
13. D. Psaltis, M. Levene, A. Pu, G. Barbastathis, and K. Curtis, "Holographic storage using shift multiplexing," *Opt. Lett.* **20**, 782–784 (1995) [doi:10.1364/OL.20.000782].
14. Y. Jeong and B. Lee, "Effect of a Random Pattern through a Multimode-Fiber Bundle on Angular and Spatial Selectivity in Volume Holograms: Experiments and Theory," *Appl. Opt.* **41**, 4085 (2002) [doi:10.1364/AO.41.004085].
15. Y. H. Kang, K. H. Kim, and B. Lee, "Angular and Speckle Multiplexing of Photorefractive Holograms by use of Fiber Speckle Patterns," *Appl. Opt.* **37**, 6969 (1998) [doi:10.1364/AO.37.006969].
16. C. Denz, G. Pauliat, G. Roosen, and T. Tschudi, "Volume hologram multiplexing using a deterministic phase encoding method," *Opt. Commun.* **85**, 171–176 (1991) [doi:10.1016/0030-4018(91)90389-U].
17. D. Gabor, "A New Microscopic Principle," *Nature* **161**, 777–778 (1948) [doi:10.1038/161777a0].
18. E. N. Leith and J. Upatnieks, "Reconstructed Wavefronts and Communication Theory*," *J. Opt. Soc. Am.* **52**, 1123 (1962) [doi:10.1364/JOSA.52.001123].
19. A. Ashkin, "OPTICALLY-INDUCED REFRACTIVE INDEX INHOMOGENEITIES IN LiNbO₃ AND LiTaO₃," *Appl. Phys. Lett.* **9**, 72 (1966) [doi:10.1063/1.1754607].
20. F. S. Chen, "HOLOGRAPHIC STORAGE IN LITHIUM NIOBATE," *Appl. Phys. Lett.* **13**, 223 (1968) [doi:10.1063/1.1652580].
21. E. G. Ramberg, "Holographic information storage," *RCA Rev* **33**, 55 (1972).
22. D. L. Staebler, "Coupled-Wave Analysis of Holographic Storage in LiNbO₃," *J. Appl. Phys.* **43**, 1042 (1972) [doi:10.1063/1.1661215].
23. D. L. Staebler, W. J. Burke, W. Phillips, and J. J. Amodei, "Multiple storage and erasure of fixed holograms in Fe-doped LiNbO₃," *Appl. Phys. Lett.* **26**, 182 (1975) [doi:10.1063/1.88108].
24. J. F. Heanue, M. C. Bashaw, and L. Hesselink, "Volume holographic storage and retrieval of digital data," *Science* **265**, 749 (1994) [doi:10.1126/science.265.5173.749].

25. Y. Taketomi, J. E. Ford, H. Sasaki, J. Ma, Y. Fainman, and S. H. Lee, "Incremental recording for photorefractive hologram multiplexing," *Opt. Lett.* **16**, 1774 (1991) [doi:10.1364/OL.16.001774].
26. L. Paraschis, "Volume holographic recording utilizing photo-initiated polymerization for nonvolatile digital data storage," PhD Thesis 4804 (2000).
27. L. Hesselink, S. S. Orlov, and M. C. Bashaw, "Holographic data storage systems," *Proc. IEEE* **92**, 1231–1280 (2004) [doi:10.1109/JPROC.2004.831212].
28. B. J. Sissom, "Miniature flexure based scanners for angle multiplexing," U.S. patent 7336409 (February 26, 2008).
29. M. R. Ayres, K. Anderson, F. Askham, and B. Sissom, "Multi-terabyte holographic data storage demonstrator," *Proc IEEE* 659–660 (2013) [doi:10.1109/IPCon.2013.6656467].
30. M. Hosaka, T. Ishii, and T. Hoshizawa, "Region-Divided Adaptive Equalization for Holographic Memory," *Proc ISOM OMB6*, (2011) [doi:10.1364/ISOM_ODS.2011.OMB6].
31. N. Kinoshita, Y. Katano, T. Muroi, N. Ishii, and N. Saito, "Playback demonstration of compressed 8K UHD TV video from holographic data storage," *Proc. SPIE* **9959–2**, (2016).
32. L. Dhar, A. Hale, H. E. Katz, M. L. Schilling, M. G. Schnoes, and F. C. Schilling, "Recording media that exhibit high dynamic range for digital holographic data storage," *Opt. Lett.* **24**, 487 (1999) [doi:10.1364/OL.24.000487].
33. A. C. Urness, W. L. Wilson, and M. R. Ayres, "Homodyne detection of holographic memory systems," *Proc. SPIE* **92010Y**, (2014) [doi:10.1117/12.2064926].
34. F. H. Mok, G. W. Burr, and D. Psaltis, "System metric for holographic memory systems," *Opt. Lett.* **21**, 896 (1996) [doi:10.1364/OL.21.000896].
35. J. Joseph and D. A. Waldman, "Homogenized Fourier transform holographic data storage using phase spatial light modulators and methods for recovery of data from the phase image," *Appl. Opt.* **45**, 6374 (2006) [doi:10.1364/AO.45.006374].
36. A. Sinha and G. Barbastathis, "Resonant holography," *Opt. Lett.* **27**, 385–387 (2002) [doi:10.1364/OL.27.000385].
37. B. E. Miller and Y. Takashima, "Formalization and experimental evaluation of cavity-enhanced holographic readout," *Proc. SPIE* **920104**, (2014) [doi:10.1117/12.2061448].

38. F. Dai and C. Gu, "Effect of Gaussian references on cross-talk noise reduction in volume holographic memory," *Opt. Lett.* **22**, 1802 (1997) [doi:10.1364/OL.22.001802].
39. K. Tian, "Three dimensional (3D) optical information processing," Thesis, Massachusetts Institute of Technology (2006).
40. L. Cao, Z. Zhao, H. Gu, Q. He, and G. Jin, "Enhancement of recording and readout for the photopolymer holographic disk system by using a conjugate structure," *Proc. SPIE* **68270X**, (2007) [doi:10.1117/12.760253].
41. H. Mikami and K. Watanabe, "Microholographic Optical Data Storage with Spatial Mode Multiplexing," *Jpn. J. Appl. Phys.* **52**, 09LD02 (2013) [doi:10.7567/JJAP.52.09LD02].
42. H. Kogelnik, "Coupled Wave Theory for Thick Hologram Gratings," *Bell Syst. Tech. J.* **48**, 2909–2947 (1969) [doi:10.1002/j.1538-7305.1969.tb01198.x].
43. R. Katayama, "Proposal for Angular Momentum Multiplexing in Microholographic Recording," *Jpn. J. Appl. Phys.* **52**, 09LD11 (2013) [doi:10.7567/JJAP.52.09LD11].
44. M. C. Bashaw, J. F. Heanue, A. Aharoni, J. F. Walkup, and L. Hesselink, "Cross-talk considerations for angular and phase-encoded multiplexing in volume holography," *J. Opt. Soc. Am. B* **11**, 1820 (1994) [doi:10.1364/JOSAB.11.001820].
45. Y. L. Korzinin, "Diffraction of a monochromatic wave of arbitrary shape by 3-D holograms with extended spatial-frequency spectrum," *Opt. Spektrosk.* **59**, 124–126 (1985).
46. Y. L. Korzinin and V. I. Sukhanov, "Diffraction efficiency of a 3-D phase hologram of a diffuse object," *Opt. Spektrosk.* **58**, 86–88 (1985).
47. Y. L. Korzinin and V. I. Sukhanov, "Light diffraction by 3-D holograms with a continuous spectrum of spatial frequencies. System of equations for coupled waves," *Opt. Spektrosk.* **56**, 467–469 (1984).
48. Y. L. Korzinin and V. I. Sukhanov, "Diffraction of light by 3-D holograms with a continuous spectrum of spatial frequencies," *Opt. Spektrosk.* **56**, 572–574 (1984).
49. A. E. Siegman, *Lasers* (University Science Books, 1986).
50. M. Jeganathan, M. C. Bashaw, and L. Hesselink, "Evolution and propagation of grating envelopes during erasure in bulk photorefractive media," *J. Opt. Soc. Am. B* **12**, 1370 (1995) [doi:10.1364/JOSAB.12.001370].

51. J. M. Heaton and L. Solymar, "Transient Energy Transfer during Hologram Formation in Photorefractive Crystals," *Opt. Acta Int. J. Opt.* **32**, 397–408 (1985) [doi:10.1080/713821751].
52. D. Maxein, J. Bückers, D. Haertle, and K. Buse, "Photorefraction in LiNbO₃:Fe crystals with femtosecond pulses at 532 nm," *Appl. Phys. B* **95**, 399–405 (2009) [doi:10.1007/s00340-009-3490-3].
53. A. Yariv and P. Yeh, *Optical Waves in Crystals Propagation and Control of Laser Radiation*, Wiley Classics Library (John Wiley & Sons, Inc., 2003).
54. F. Askham, M. R. Ayres, and A. C. Urness, "High dynamic range holographic data storage media," *Proc. SPIE* **9587–6**, (2015) [doi:10.1117/12.2188794].
55. M. R. Gleeson, J. T. Sheridan, F.-K. Bruder, T. Rölle, H. Berneth, M.-S. Weiser, and T. Fäcke, "Comparison of a new self developing photopolymer with AA/PVA based photopolymer utilizing the NPDD model," *Opt. Express* **19**, 26325 (2011) [doi:10.1364/OE.19.026325].
56. T. Ishii, K. Shimada, T. Hoshizawa, and Y. Takashima, "Analysis of vibration effects on holographic data storage system," *Jpn. J. Appl. Phys.* **54**, 09MA04 (2015) [doi:10.7567/JJAP.54.09MA04].
57. K. Shimada, T. Ishii, T. Hoshizawa, and Y. Takashima, "New optical modeling and optical compensation for mechanical instabilities on holographic data storage system using time averaged holography," *Jpn. J. Appl. Phys.* **54**, (2015) [doi:10.7567/JJAP.54.09MA01].
58. A. Hoskins, B. Ihas, K. Anderson, and K. Curtis, "Monocular Architecture," *Jpn. J. Appl. Phys.* **47**, 5912–5914 (2008) [doi:10.1143/JJAP.47.5912].
59. C. Sigel and M. L. Leonhardt, "System and method for providing gain and thresholding to a holographic data parallel recording and replication system incorporating independent angular address assignment," U.S. patent US7187481 B1 (March 6, 2007).
60. A. E. Siegman, "Lasers," in *Lasers* (University Science Books, 1986), pp. 413–426, 642–648, 690.
61. J. W. Goodman, "Introduction to Fourier Optics," in *Introduction to Fourier Optics*, 3rd ed. (Roberts & Company Publishers, 2005), pp. 107–108.
62. J. Kühn and P. Patapis, "Digital adaptive coronagraphy using SLMs: promising prospects of a novel approach, including high-contrast imaging of multiple stars systems," *Proc. SPIE* **99122M**, (2016) [doi:10.1117/12.2232660].

63. "HOLOEYE Photonics AG » LC 2012 Spatial Light Modulator (transmissive)," <http://holoeye.com/spatial-light-modulators/lc-2012-spatial-light-modulator/>.
64. T. Hoshizawa, K. Shimada, K. Fujita, and Y. Tada, "Practical angular-multiplexing holographic data storage system with 2 terabyte capacity and 1 gigabit transfer rate," *Jpn. J. Appl. Phys.* **55**, 09SA06 (2016) [doi:10.7567/JJAP.55.09SA06].
65. R. W. P. Drever, J. L. Hall, F. V. Kowalski, J. Hough, G. M. Ford, A. J. Munley, and H. Ward, "Laser phase and frequency stabilization using an optical resonator," *Appl. Phys. B Photophysics Laser Chem.* **31**, 97–105 (1983) [doi:10.1007/BF00702605].
66. T. W. Hansch and B. Couillaud, "Laser frequency stabilization by polarization spectroscopy of a reflecting reference cavity," *Opt. Commun.* **35**, 441–444 (1980) [doi:10.1016/0030-4018(80)90069-3].